Geophysical Journal International

Geophys. J. Int. (2019) **216,** 1901–1918
Advance Access publication 2018 December 11
GJI Geomagnetism, rock magnetism and paleomagnetism

doi: 10.1093/gji/ggy515

Local averages of the core–mantle boundary magnetic field from satellite observations

Magnus D. Hammer and Christopher C. Finlay

Division of Geomagnetism, Technical University of Denmark - DTU Space, Kgs. Lyngby, Denmark. E-mail: magdh@space.dtu.dk

Accepted 2018 December 6. Received 2018 November 16; in original form 2018 July 02

SUMMARY

We introduce a formalism for estimating local spatial averages of the core–mantle boundary (CMB) radial magnetic field and its time derivatives, based on magnetic field observations collected by low-Earth-orbit satellites. This provides a useful alternative to conventional core field modelling based on global spherical harmonic basis functions, where noise in the polar regions maps into all harmonics, and model regularization and spectral truncation are required. A powerful perspective offered by the proposed technique is formal appraisal of the spatial resolution and variance of the resulting field averages. We use the Green's functions for the Neumann boundary value problem to link the satellite observations to the radial magnetic field on the CMB and estimate field averages using a modified Backus–Gilbert inversion approach. Our approach builds on the Subtractive Optimally Localized Averages (SOLA) method developed in helioseismology, that seeks averaging kernels as close as possible to a chosen target kernel. We are able to account for both internal and external field sources and can incorporate data error covariance information, for example describing along-track serial error correlation. As a proof of concept we present a global map collecting local estimates of the radial main field (MF) constructed on a grid at the CMB with one degree spacing in latitude and longitude, derived from 1 month of three component vector magnetic field data collected by the *Swarm* satellite trio, using data from dark and geomagnetically quiet times. Using sums and differences of the field components taken along track and in the east–west direction we obtain estimates with spatial resolution kernel widths varying between 18° and 54° depending on the latitude, and a standard deviation of approximately 10 μT (i.e. 5 per cent of the mean CMB field amplitude). The morphology of our CMB radial field map agrees well with results from conventional spherical harmonic field models. In a second application, we determine local estimates of the average rate of change, or secular variation (SV), of the radial field at the CMB, initially considering 2-yr time windows, and performing the analysis on data collected by either the *Swarm* or CHAMP satellites. We obtain stable local estimates of the SV at the CMB, and present maps of estimates with averaging kernel widths of approximately 42°, 33° and 30° on the equator, with corresponding standard derivations of 0.25, 2.5 and 5 μT yr^{-1}. By subtracting SV estimates constructed at different epochs we are able to calculate the local aggregated secular acceleration (SA) and to study its time changes. Differencing SV estimates 2 yr apart, and considering an averaging kernel width of 42° on the equator, we obtain SA maps similar to those found in the CHAOS-6-x7 field model truncated at SH degree 10. Using our approach we are able to directly control the width of the spatial averaging kernel and the length of the time window, enabling us to directly study the robustness of the inferred SA. Pushing to higher resolution in time, considering 1 yr differences of SV estimates constructed using 1 yr windows, we are able to track the evolution of coherent SA structures in time-longitude plots at the equator. At 25°W in mid 2007 we find a distinctive SA 'cross-over' event, with strong, oppositely signed and adjacent, SA features rapidly changing sign within a year. Our method is well suited for studying such spatio-temporally localized SA events at high resolution; there will be further opportunities for such investigations as the time-series of data provided by the *Swarm* mission lengthens.

Key words: Rapid time variations; Satellite magnetics; Inverse theory.

1 INTRODUCTION

The ability to construct reliable estimates of the core-generated magnetic field, tracking its morphology and time evolution, is essential in efforts to improve our knowledge of core dynamics. With the advent of the low-Earth-orbit CHAMP and *Swarm* satellite missions collecting magnetic measurements over multiple years, it has become possible to image small scale features of the core field that exhibit rapid temporal variations (Lesur *et al.* 2008; Olsen & Mandea 2008; Finlay *et al.* 2016). The first and second time derivative of the main field undergoes subdecadal changes that may be probed down to a period of about 1 yr (Chulliat *et al.* 2015). New techniques have been developed that use spatial differences of the magnetic field observations in order to to enhance the recovery of small scale field features, since compared to using vector data, they are less sensitive to unmodelled large-scale external field contamination (Kotsiaros *et al.* 2015; Olsen *et al.* 2015; Finlay *et al.* 2016). Spherical harmonic (SH) models derived using *Swarm* observations have shown that the first time derivative of the field, or secular variation (SV), can be obtained up to approximately SH degree 11 from 1 yr of measurements (Olsen *et al.* 2015, 2016). Studies of geodynamo simulations have also recently suggested that the second time derivative of the field, or secular acceleration (SA), might be expected to exhibit distinctive equatorial localization (Aubert 2018). Moreover, considering 3-yr data time windows, pulse like features in the radial SA at the core–mantle boundary (CMB) concentrated along the geographical equator, have recently been observed (Chulliat & Maus 2014; Chulliat *et al.* 2015) possibly indicative of a wave propagating or arriving at the core surface. The basic structure of the SA at short length and timescales, and the details of the responsible core dynamics are however still unclear and further investigations are urgently needed.

Assuming the region between the CMB and the observation site is an insulator, the magnetic field can be described by the gradient of a scalar magnetic potential. In the conventional, so-called construction, approach to field modelling the potential is represented on a global scale using a truncated SH expansion determined using a least-squares solution (Langel 1987; Parker 1994) that is often also regularized in order to obtain stable solutions at the CMB (Bloxham *et al.* 1989). Here we use the term regularization to denote the modification of the least-squares solution to the inverse problem such that a global norm of the model parameters is added to the data misfit norm in the cost function being minimized. Since the SH functions are of global support, assuming equal data errors, they give equal weight to the entire data set assigning isotropic resolution. Regularized B-splines are often used to describe the model time dependence; the temporal regularization modifies the spline functions in a non-uniform manner influencing higher SH degrees the most (Constable & Parker 1988; Olsen *et al.* 2009). Moreover, model uncertainties are usually not provided and validation typically relies on comparing models constructed using different data selection schemes, external field parametrizations and regularizations.

Various alternatives to SH modelling have been investigated for studying the CMB magnetic field, for instance constructing models based on icosodedral grids for the radial field at the core surface that can be forced to satisfy necessary conditions for frozen-flux and a magnetostrophic force balance implemented via topology preservation constraints (Constable *et al.* 1993; Jackson *et al.* 2007). Techniques such as harmonic splines introduced by Shure *et al.* (1982) and Parker & Shure (1982), a wavelet approach developed by Holschneider *et al.* (2003), and Slepian functions (Plattner & Simons 2017) have also been explored. Most recently, Holschneider *et al.* (2016) have introduced an attractive new technique, based on specifying appropriate correlation functions for internal and external sources, that has been used by Lesur *et al.* (2017) to determine the Gauss coefficients for the SV from ground observatory monthly means between 1957 and 2014.

A difficulty with core field studies is that the CMB spectra of the SV and SA signals are blue (i.e. power increases with SH degree). Although studies have shown encouraging coherence in field maps as SH truncation degree is increased (Holme *et al.* 2011; Aubert 2018) care is needed when interpreting the resulting fields. Furthermore, it has been argued that the temporal spectra of the core field is such that higher order time derivatives of the field, in particular the SA, may be formally undefined as the time window used to estimate them goes towards zero (Gillet *et al.* 2013; Bouligand *et al.* 2016; Lesur *et al.* 2017). Pushing towards signal recovery on smaller length scales and shorter timescales, careful appraisal, comprising of resolution analysis and variance estimation, is required in order to assess limitations of the data and to establish the validity of features of interest in field reconstruction.

Here we propose another approach to the above problems. We adopt a formalism for estimating the CMB radial field which is not founded on spherical harmonics, thus is free of signal truncation in the spectral domain, relying instead on spatial averaging of the field. We investigate the inverse problem using the Backus–Gilbert philosophy of appraisal (Backus and Gilbert, 1968; Backus and Gilbert, 1970; Parker, 1977; Oldenburg, 1984), which provides the only unique information directly obtainable from the data, thereby enabling us to explore whether all constructed models contain certain spatial field features of interest. In the case of accurate data, any linear data combination will give a uniquely specified value of the magnetic field; this is equivalent to an unique spatial average value, determined by the inner product of an averaging kernel with the true model around some location of interest (Oldenburg 1984; Pujol 2013). In the case of inaccurate data, a variance is assigned to the estimated average and a trade-off arises between spatial resolution and variance. It should be stressed that the obtained average will in general not fit the original data, nor is it directly supposed to. Any model obtained (e.g. in the least-squares sense) which reproduces the data must attain this estimated average. It is relevant to note here that regularized least-square solutions are biased towards a background model that is often assumed to be zero. A result of this is that rows of the model resolution matrix can sum to less than 1 (see e.g. Nolet 2008, pp. 277–281). Another undesirable effect of regularization is to produce model covariance estimates that can be unrealistically small. In contrast Backus–Gilbert estimates are unbiased (the averaging kernels integrate to 1) and the variances of the estimated averages are meaningful. The Backus–Gilbert philosophy is thus fundamentally different from that of the conventional regularized inversion construction approach, and it has been applied to a wide range of geophysical topics (e.g. Tanimoto 1985; Masters & Gubbins

2003; Pujol 2013). In geomagnetism, Whaler & Gubbins (1981) used the Backus–Gilbert formalism to invert for an average vertical field component at the CMB, taking Gauss coefficients derived from 80 ground observatories as data. Later Whaler (1984) used Backus–Gilbert theory to estimate null-flux patch integrals of the radial SV component. Modifications to the original Backus–Gilbert method (referred to as quelling by its authors and mollifying in mathematical literature), resembling the so-called Dirichlet deltaness criterion, have been developed independently by Louis & Maass (1990) and Pijpers & Thompson (1992) in helioseismology, and termed Subtractive Optimally Localized Averages (SOLA) by the latter. The SOLA approach estimates the coefficients of linear data combinations by minimizing a norm measuring the squared distance between the averaging kernel and some chosen target kernel.

Here, we implement the SOLA technique such that at specified locations on the CMB, local spatial averages of the radial field are calculated, that then allow for appraisal to be carried out. To do this we represent the magnetic potential, which satisfies the Neumann boundary value problem for the Laplace equation, using the Green's function method so that the CMB field is related to the observations via appropriate Green's functions (e.g. Gubbins & Roberts 1983). A general formalism is presented where the potential is described by both internal and external source contributions. Section 2 provides a description of the selection criteria and processing procedures for the data used in our chosen applications. Section 3.1 describes the potential field formulation relating the radial magnetic field at the source regions to the satellite magnetic data. In Section 3.2, aspects of the SOLA approach to the inverse problem are described, allowing for estimates of the field to be determined as localized spatial averages. Section 3.3 considers our numerical implementation of the theory and Section 3.4 describes in detail how appraisal of the results can be carried out. Section 4 contains results from applications based on (i) using *Swarm* data to estimate the field at the CMB and (ii) using *Swarm* and CHAMP data to estimate the secular variation, and the accumulated secular acceleration over chosen time windows, also at the CMB. Discussions and conclusions are given in Section 5.

2 DATA

We take CHAMP vector magnetometer measurements from 2000 July 19 to 2010 September 1 and *Swarm* vector magnetometer measurements, from all three satellites (*Alpha*, *Bravo*, *Charlie*), from 2013 December 1 up to the end of August 2018. We extract samples every 15 s from low rate (5 Hz for CHAMP and 1 Hz for *Swarm*) calibrated magnetic field data in the Vector Field Magnetometer (VFM) frame (in units of nT) provided by the CHAMP MAG-L3 and *Swarm* Level 1b MAG-L version 0505 data products. The VFM data are then transformed into an Earth-Centred Earth-Fixed (ECEF) local Cartesian North-East-Centre (NEC) coordinate frame. This is done by data alignment in which the VFM data are rotated into the Common Reference Frame (CRF) of the star tracker using the Euler rotation angles as determined by the CHAOS-6-x7 model (an extension of the CHAOS-6 model using *Swarm* data and ground observation data up until the end of August 2018, http://www.spacecenter.dk/files /magnetic-models/CHAOS-6/). We reject measurements for known disturbed days where satellite manoeuvres took place and remove gross data outliers for which the vector field components deviate more than 500 nT from CHAOS-6-x7 field predictions. Based on previous experience (e.g. Olsen *et al.* 2015; Finlay *et al.* 2016) we adopt the following selection criteria: (1) only dark region data requiring the sun to be at least 10° below horizon in order to reduced ionospheric field contamination; (2) for quiet time conditions we require the geomagnetic planetary activity index $K_p < 2^o$; (3) for the magnethospheric ring current and its Earth induced contribution the *RC* disturbance index is required to have $|d\mathrm{RC}/dt| < 2$ nT hr^{-1} (Olsen *et al.* 2014) and (4) restricting the merging electric field at the magnetopause such that $E_m \leq 0.8$ mV m^{-1} with $E_m = 0.33 v^{4/3} B_t^{2/3} \sin(|\Theta|/2)$ where v is the solar wind speed, $\Theta = \arctan(B_y/B_z)$ and $B_t = \sqrt{B_y^2 + B_z^2}$ is the magnitude of the interplanetary magnetic field (IMF) having components in the geocentric solar magnetospheric (GSM) coordinate y–z plane, calculated using 2 hourly means based on 1-min values of the IMF and solar wind extracted form the OMNI database (http://omniweb.gsfc.nasa.gov); (5) requiring that IMF $B_Z > 0$nT and IMF $|B_Y| < 6$nT in order to reduce substorm auroral electrojet contamination originating from field-aligned currents (Ritter *et al.* 2004). Finally, CHAOS-6-x7 model estimates of the crustal field for SH degrees 14–120 and the external magnetospheric (plus induced) field together with the CM4 (Sabaka *et al.* 2004) estimates of the ionospheric field and its induced counterpart scaled by the F10.7 solar flux index are subtracted.

We work with magnetic vector field data as well as with sums and differences of the magnetic field components $B_k = \hat{\mathbf{k}} \cdot \mathbf{B}(\mathbf{r})$ in geographic spherical polar coordinates where $(k = r, \theta, \phi)$, such that Δd_k and Σd_k are data differences and sums, respectively. We construct along-track (AT) and east–west (EW) differences $\Delta d_k = (\Delta d_k^{\mathrm{AT}}, \Delta d_k^{\mathrm{EW}})$, and data sums $\Sigma d_k = (\Sigma d_k^{\mathrm{AT}}, \Sigma d_k^{\mathrm{EW}})$. Note that it is necessary to consider data sums as well as differences to ensure sufficient information on longer wavelengths. The along-track differences are calculated using 15 s differences $\Delta d_k^{\mathrm{AT}} = [B_k(\mathbf{r}, t) - B_k(\mathbf{r} + \delta\mathbf{r}, t + 15s)]$. With a satellite speed of ≈7.7 km s^{-1} this corresponds to an along-track distance of 115 km (Olsen *et al.* 2015). The along-track summations are calculated as $\Sigma d_k^{AT} = [B_k(\mathbf{r}, t) + B_k(\mathbf{r} + \delta\mathbf{r}, t + 15s)]/2$. The EW differences are calculated as $\Delta d_k^{\mathrm{EW}} = [B_k^{\mathrm{SWA}}(\mathbf{r}_1, t_1) - B_k^{\mathrm{SWC}}(\mathbf{r}_2, t_2)]$ having an EW orbit separation between the *Swarm Alpha* (SWA) and *Charlie* (SWC) satellites of ≈1.4° (corresponding to 155 km) at the equator (Olsen *et al.* 2015). The EW summation is calculated as $\Sigma d_k^{\mathrm{EW}} = [B_k^{\mathrm{SWA}}(\mathbf{r}_1, t_1) + B_k^{\mathrm{SWC}}(\mathbf{r}_2, t_2)]/2$. For a particular orbit of *Alpha* we select the corresponding *Charlie* data to be the one closest in colatitude such that $|\Delta t| = |t_1 - t_2| < 50$ s.

We adopt error estimates that depend on quasi-dipole (QD) latitude (Richmond 1995) and make use of robust (Huber) weights appropriate for a long tailed error distribution (Constable 1988). First, using all available data d_i within bins of 2° QD latitude, we determine separately

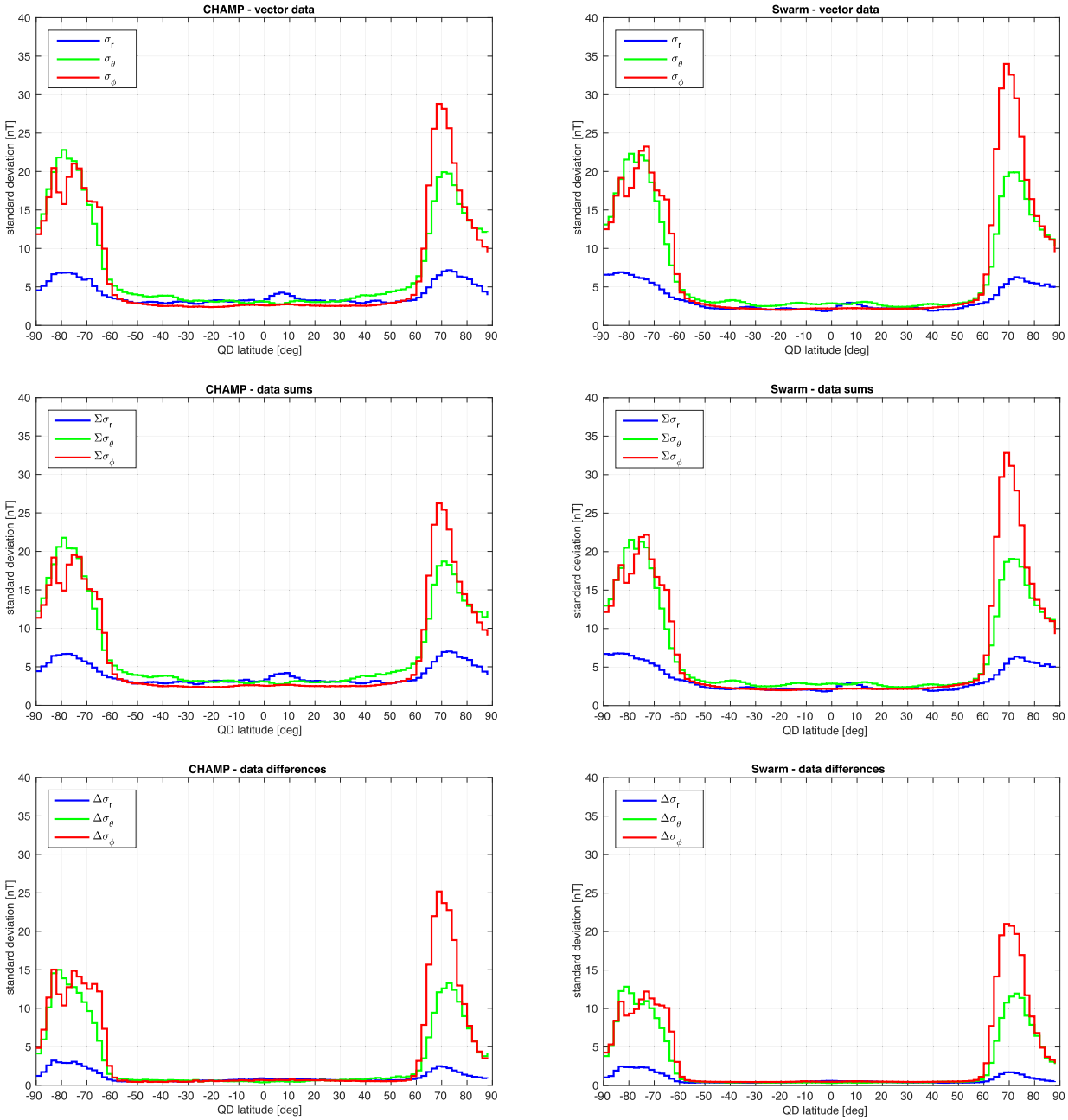

Figure 1. Latitude-dependent Huber weighted standard deviations in 2° bands (Northern hemisphere having positive QD) for CHAMP data (left-hand figures) and *Swarm* data (right-hand figures). Top panels: using vector data, centre using data sums and bottom panels using data differences.

for each field component and their sums and differences for each satellite standard deviations, $\sigma(\theta_{QD})$ according to

$$\sigma(\theta_{QD}) = \sqrt{\frac{\sum_i w_i(\epsilon_i - \mu)^2}{\sum w_i}}, \tag{1}$$

where $(i = 1, ..., D)$ denotes the data elements within the bin, ε_i are the residuals to the CHAOS-6-x7 field predictions for SH degrees 1–13, μ is the weighted mean residual and w_i are the weights $w_i = \min(c_w/\varepsilon_i, 1)$ with a selected breakpoint $c_w = 1.5$ (e.g. Constable 1988). Considering separately each field component and their sums and differences for each satellite, weighted data error variances for data element n, where $(n = 1, ..., N)$, were specified as $\sigma^2_{w,n}(\theta_{QD}) = \sigma^2(\theta_{QD})/w_n$, where $\sigma(\Theta_{QD})$ is the standard deviation for the QD latitude, data element and satellite in question from (1), and w_n is the Huber weight for data element n. Fig. 1 presents these latitude-dependent, Huber weighted, error estimates as a function of QD latitude for CHAMP and *Swarm* vector data as well as data differences and sums. Large data error estimates are confined to polar region latitudes (i.e. QD latitudes 60° to 90° and −60° to −90° for the northern and southern polar regions, respectively). Data error estimates are larger for the horizontal components exhibiting a noticeable asymmetry between the northern and southern polar regions, a feature also observed in previous studies (Kotsiaros *et al.* 2015).

3 METHODOLOGY

3.1 Potential field formulation

Measurements of the magnetic field are made at geocentric radius r in the volume V of a spherical shell bounded as $r_c \leq r \leq r_m$, that is assumed to contain no magnetization and no electric nor displacement currents. That is, V is bounded by a surface S having the disconnected parts S_C and S_M; S_C is closed and finite at radius r_c and S_M is closed and finite at radius r_m. In the ECEF frame the magnetic vector field $\mathbf{B}$ of this volume can be then represented by the gradient of a scalar potential function, $\mathbf{B} = -\nabla\psi$, which fulfils the Laplace equation $\nabla^2\psi = 0$ (e.g. Backus *et al.* 1996). The Laplace equation subject to prescribed values of the outward normal derivative on S_C/S_M is known, respectively, as the exterior/interior Neumann boundary value problem. Care is needed for geomagnetists with the notation here; the 'exterior' problem involves fields produced by internal sources while the 'interior' problem involves fields produced by external sources. Because Maxwell's equations are linear with respect to the sources, the total field is a superposition of fields produced by the two sources, that is $\mathbf{B} = \mathbf{B}_C + \mathbf{B}_M = -\nabla\psi_C - \nabla\psi_M$, where ψ_C here describes the internal (core) sources and ψ_M describes the external (large-scale magnetospheric) sources. From the Laplace equation, Green's identities can be derived from which Green's second identity allows a solution for the potential to be formulated. The uniqueness theorem then assures that the solution found is unique up to an additive constant (e.g. Barton 1989).

In the ECEF geographic spherical polar coordinate system the magnetic field components ($k = r, \theta, \phi$) at some observation location, $\mathbf{r}$, are linked to the radial field at surfaces S_C and S_M having position vector, $\mathbf{r}'$, which we take to be at the CMB ($r' = r_c = 3480$ km) and at the magnetosphere ($r' = r_m = 4r_a$) (where $r_a = 6371.2$ km is the mean Earth reference radius), respectively, by the gradient of the potential

$$\begin{aligned} B_k(\mathbf{r}, t) &= -\oint_{S_C} \nabla_k N_C(\mathbf{r}|\mathbf{r}') B_r(\mathbf{r}', t) r_c^2 \mathrm{d}S'_C - \oint_{S_M} \nabla_k N_M(\mathbf{r}|\mathbf{r}') B_r(\mathbf{r}', t) r_m^2 \mathrm{d}S'_M \\ &= \oint_{S_C} G_{C,k}(\mathbf{r}|\mathbf{r}') B_r(\mathbf{r}', t) \mathrm{d}S'_C + \oint_{S_M} G_{M,k}(\mathbf{r}|\mathbf{r}') B_r(\mathbf{r}', t) \mathrm{d}S'_M, \end{aligned} \tag{2}$$

where $\mathrm{d}S'_C, \mathrm{d}S'_M = \sin\theta' \mathrm{d}\theta' \mathrm{d}\phi'$. Eq. (2) is a linear system which consists of a sum of two homogeneous Fredholm integral equations of the first kind, for the unknown radial fields at the CMB and the magnetosphere. $N_C(\mathbf{r}|\mathbf{r}')$, having absorbed the term r_c^2, is the exterior Neumann Green's function and $N_M(\mathbf{r}|\mathbf{r}')$, having absorbed the term r_m^2, is the interior Neumann Green's function (Barton 1989, p. 412). The directional derivatives of the Green's functions (with respect to $\mathbf{r}$), $G_{C,k}(\mathbf{r}|\mathbf{r}')$ and $G_{M,k}(\mathbf{r}|\mathbf{r}')$, are known as the data kernels and can be derived using the chain rule (Gubbins & Roberts 1983). The exterior data kernels (associated with internal sources) are given by

$$G_{C,r} = -\frac{\partial N_C}{\partial r} = \frac{1}{4\pi} \frac{h^2(1-h^2)}{f^3} \tag{3}$$

$$G_{C,\theta} = -\frac{1}{r}\frac{\partial N_C}{\partial \theta} = -\frac{1}{r}\frac{\partial N_C}{\partial \mu}\frac{\partial \mu}{\partial \theta} = -\frac{1}{r}\frac{\partial N_C}{\partial \mu}[\cos\theta \sin\theta' \cos(\phi - \phi') - \sin\theta \cos\theta'] \tag{4}$$

$$G_{C,\phi} = -\frac{1}{r\sin\theta}\frac{\partial N_C}{\partial \phi} = -\frac{1}{r\sin\theta}\frac{\partial N_C}{\partial \mu}\frac{\partial \mu}{\partial \phi} = \frac{1}{r}\frac{\partial N_C}{\partial \mu}[\sin\theta' \sin(\phi - \phi')], \tag{5}$$

where the derivative with respect to μ is

$$\frac{1}{r}\frac{\partial N_C}{\partial \mu} = \frac{h}{4\pi}\left[\frac{1 - 2h\mu + 3h^2}{f^3} + \frac{\mu}{f(f + h - \mu)} - \frac{1}{1-\mu}\right]. \tag{6}$$

The corresponding interior data kernels (associated with external sources) are given by

$$G_{M,r} = -\frac{\partial N_M}{\partial r} = \frac{1}{4\pi}\left[h + \frac{h^2(1-h)}{f^3}\right] \tag{7}$$

$$G_{M,\theta} = -\frac{1}{r}\frac{\partial N_M}{\partial \theta} = -\frac{1}{r}\frac{\partial N_M}{\partial \mu}\frac{\partial \mu}{\partial \theta} = -\frac{1}{r}\frac{\partial N_M}{\partial \mu}[\cos\theta \sin\theta' \cos(\phi - \phi') - \sin\theta \cos\theta'] \tag{8}$$

$$G_{M,\phi} = -\frac{1}{r\sin\theta}\frac{\partial N_M}{\partial \phi} = -\frac{1}{r\sin\theta}\frac{\partial N_M}{\partial \mu}\frac{\partial \mu}{\partial \phi} = \frac{1}{r}\frac{\partial N_M}{\partial \mu}[\sin\theta' \sin(\phi - \phi')], \tag{9}$$

where the derivative with respect to μ is

$$\frac{1}{r}\frac{\partial N_M}{\partial \mu} = -\frac{h}{4\pi}\left[\frac{2h^2}{f^3} + \frac{r'/f}{r' - \mu r + rf)}\right]. \tag{10}$$

In the above expressions we have used $h = r'/r, f = R/r$, $R = \sqrt{r^2 + r'^2 - 2rr'\mu}$ and $\mu = \cos\gamma = \cos\theta\cos\theta' + \sin\theta\sin\theta'\cos(\phi - \phi')$, γ being the angular distance. Note that in Gubbins & Roberts (1983) these expressions include the monopole term that was removed by Constable *et al.* (1993) but we retain this terms as it proves useful when constructing localised Backus–Gilbert averaging kernels (see Section 3.2).

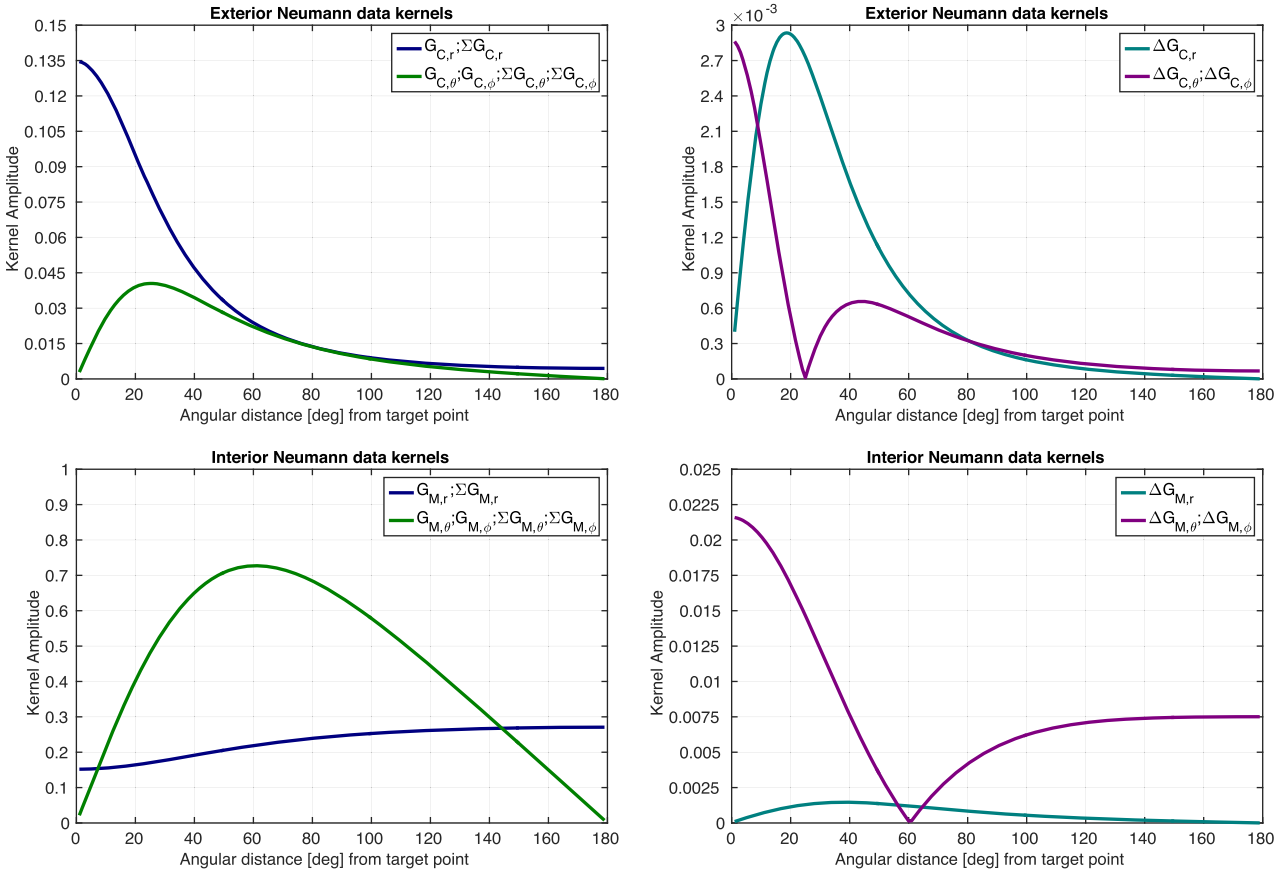

Figure 2. Sensitivity of satellite measurements to the CMB field versus angular distance from target point as determined by data kernels using an observation altitude of $r_{obs} = r_a + 400$ km. Top panel: exterior data kernels plotted using a source radius $r' = r_c$. Bottom panel: interior data kernels plotted using a source radius $r' = 4r_a$.

3.2 Modified Backus–Gilbert method

Applying the Backus–Gilbert formalism to the linear system (2), we determine an estimate, $\widehat{B}_r$, of the radial field as a spatial average that is optimally localized around a particular location and time of interest $(\mathbf{r}_0, t_0) = (r_c, \theta_0, \phi_0, t_0)$. The estimate is an inner product of the field of interest and some averaging kernel, and can be written as a linear combination of the data (Backus & Gilbert 1968, Backus & Gilbert 1970)

$$\widehat{B}_r(\mathbf{r}_0, t_0|\mathbf{r}_n, t_n) = \sum_n^N q_n(\mathbf{r}_0, t_0) d_n(\mathbf{r}, t), \tag{11}$$

where $(n = 1, ..., N)$ is the total number of data used over the specified time span. Data d_n for a particular position $\mathbf{r}_n$ at times t_n and field component k, are related to the radial field $B_r(\mathbf{r}', t)$ at the CMB and the magnetosphere as in (2), but we also allow the field at the core surface to be time-dependent by adopting a first order Taylor expansion assumed valid close to a reference time t_0

$$\begin{aligned} d_k(\mathbf{r}_n, t_n) &= \oint_{S_C} G^*_{C,k}(\mathbf{r}_n|\mathbf{r}') B_r(\mathbf{r}', t_n) \mathrm{d}S'_C + \oint_{S_M} G^*_{M,k}(\mathbf{r}_n|\mathbf{r}') B_r(\mathbf{r}', t_n) \mathrm{d}S'_M \\ &\approx \oint_{S_C} G^*_{C,k}(\mathbf{r}_n|\mathbf{r}') \left[B_r(\mathbf{r}', t_0) + \dot{B}_r(\mathbf{r}', t_0) \Delta t_n \right] \mathrm{d}S'_C + \oint_{S_M} G^*_{M,k}(\mathbf{r}_n|\mathbf{r}') B_r(\mathbf{r}', t_n) \mathrm{d}S'_M, \end{aligned} \tag{12}$$

where $G^*_k(\mathbf{r}_n|\mathbf{r}')$ are the appropriate data kernels for the vector field components or their sums and differences. The time difference to some given reference time t_{ref} is $\Delta t_n = t_n - t_{ref}$. Here we select the reference time to be the target time, that is $t_{ref} = t_0$. The first order Taylor expansion adopted is sufficient given the short time windows considered here, more complex time parametrizations are also in principle possible. Fig. 2 presents examples of the exterior and interior data kernels for vector data denoted $\{G_{C,k}; G_{M,k}\}$, data sums denoted $\{\sum G_{C,k}; \sum G_{M,k}\}$ and data differences denoted $\{\Delta G_{C,k}; \Delta G_{M,k}\}$, using an observation altitude above ground of 400 km. The plots illustrate how a given measurement samples the CMB and the magnetosphere ; for instance the radial data d_r samples the radial core field, via $G_{C,r}$, most strongly directly below the observation site while the radial difference Δd_r samples the radial core field, via $\Delta G_{C,r} = [G_{C,r}(\mathbf{r}_1|\mathbf{r}') - G_{C,r}(\mathbf{r}_2|\mathbf{r}')]$, most strongly at an angular distance of approximately 20° having no sensitivity directly beneath the observation site.

Inserting (12), via the chosen data, into (11), the estimate at target time t_0 can be written as

$$\widehat{B}_r(\mathbf{r}_0, t_0|\mathbf{r}_n, t_n) = \oint_{S_C} \sum_n^N q_n G^*_{C,k}(\mathbf{r}_n|\mathbf{r}') B_r(\mathbf{r}', t_0) \mathrm{d}S'_C + \oint_{S_C} \sum_n^N q_n G^*_{C,k}(\mathbf{r}_n|\mathbf{r}') \dot{B}_r(\mathbf{r}', t_0) \Delta t_n \mathrm{d}S'_C + \oint_{S_M} \sum_n^N q_n G^*_{M,k}(\mathbf{r}_n|\mathbf{r}') B_r(\mathbf{r}', t_n) \mathrm{d}S'_M. \quad (13)$$

The weighting coefficients, q_n, define spatial averaging kernels that are linear combinations of the data kernels

$$\mathcal{K}_C(\mathbf{r}_0, t_0|\mathbf{r}', t) = \sum_n^N q_n(\mathbf{r}_0, t_0) G^*_C(\mathbf{r}_n|\mathbf{r}') \quad (14)$$

$$\mathcal{K}_{\dot{C}}(\mathbf{r}_0, t_0|\mathbf{r}', t) = \sum_n^N q_n(\mathbf{r}_0, t_0) G^*_C(\mathbf{r}_n|\mathbf{r}') \Delta t_n \quad (15)$$

$$\mathcal{K}_M(\mathbf{r}_0, t_0|\mathbf{r}', t) = \sum_n^N q_n(\mathbf{r}_0, t_0) G^*_M(\mathbf{r}_n|\mathbf{r}'), \quad (16)$$

where the notation $\mathcal{K}_{\dot{C}}$ highlights the inclusion of the time difference Δt_n from the Taylor expansion to the data kernel defining $G^*_{\dot{C}} = G^*_C \Delta t_n$. Thus the estimated radial field consists of spatial integrals over the source spheres of the true field convolved with averaging kernels

$$\widehat{B}_r(\mathbf{r}_0, t_0|\mathbf{r}_n, t_n) = \oint_{S_C} \mathcal{K}_C(\mathbf{r}_0, t_0|\mathbf{r}', t) B_r(\mathbf{r}', t_0) \mathrm{d}S'_C + \oint_{S_C} \mathcal{K}_{\dot{C}}(\mathbf{r}_0, t_0|\mathbf{r}', t) \dot{B}_r(\mathbf{r}', t_0) \mathrm{d}S'_C + \oint_{S_M} \mathcal{K}_M(\mathbf{r}_0, t_0|\mathbf{r}', t) B_r(\mathbf{r}', t) \mathrm{d}S'_M. \quad (17)$$

Varying the coefficients, q_n, changes the shape of the averaging kernels. Incorporating the time differences in the averaging kernel may be thought of as assigning temporal weights to that kernel. These weights may act in such a way as to produce SV field estimates; for instance, selecting data from a time window of 2 yr centred on the reference time will assign equal weights having opposite signs relative to t_0 such that field differences are computed. In order for the estimate to represent a meaningful physical average and to avoid a biased result, a normalization of the averaging kernels is implemented requiring a unimodular constraint to be fulfilled

$$\oint_{S_C} \mathcal{K}_C(\mathbf{r}_0, t_0|\mathbf{r}', t) \mathrm{d}S'_C + \oint_{S_C} \mathcal{K}_{\dot{C}}(\mathbf{r}_0, t_0|\mathbf{r}', t) \mathrm{d}S'_C + \oint_{S_M} \mathcal{K}_M(\mathbf{r}_0, t_0|\mathbf{r}', t) \mathrm{d}S'_M = 1. \quad (18)$$

In practice, we want the term of interest to integrate to one and the other terms to be zero. Seeking the radial main field, data from narrow time windows are used such that the second term is neglected and the third term should integrate to zeros. Seeking an estimate of the temporal radial field change during a selected time window, the first and last terms should integrate to zero while the second term should integrate to one. It should be noted that the monopole term was retained in (3–10). This is necessary in order to prevent the averaging kernel from integrating to zero in violation of the unimodular constraint (Whaler 1984).

A generalized formulation of the Backus–Gilbert method, known as Optimally Localized Averages (OLA) involves minimizing some suitable measure of the averaging kernel (Pijpers & Thompson 1992; Pujol 2013)

$$\oint_S \mathcal{J}(\mathbf{r}_0)[\mathcal{K}(\mathbf{r}_0|\mathbf{r}') - \mathcal{T}(\mathbf{r}_0|\mathbf{r}')]^2 \mathrm{d}S', \quad (19)$$

where $\mathcal{J}$ is a weight function and $\mathcal{T}$ is a target function. Selecting ($\mathcal{J} = 12(\mathbf{r} - \mathbf{r}_0)^2; \mathcal{T} = 0$) corresponds to the original Backus–Gilbert approach of minimizing a product of the weight function and averaging kernel, also known as Multiplicative OLA (MOLA). The Subtractive OLA (SOLA) approach, pioneered and publicized in a series of papers by Pijpers & Thompson (1992, 1994), instead uses a norm measuring the squared distance between the averaging kernel, $\mathcal{K}$, and some chosen target function, $\mathcal{T} \neq 0$, taking $\mathcal{J} = 1$. The advantage of using SOLA over the MOLA, is that significant computational time can be saved when performing calculation of multiple estimates, see Section 3.3 for more details. For the target kernel, $\mathcal{T}$, we choose a Fisher function on a sphere using the angular distance $\Psi(\mathbf{r}_0|\mathbf{r}')$

$$\mathcal{T}(\Psi) = \frac{\kappa}{4\pi \sinh\kappa} e^{\kappa \cos\Psi}, \quad (20)$$

where κ is the width of the distribution (Fisher 1953). Here $\cos\Psi = \cos\theta_0 \cos\theta' + \sin_0\theta \sin\theta' \cos(\phi_0 - \phi')$, Ψ being the angular distance between points $\mathbf{r}_0$ and $\mathbf{r}'$ on the sphere. We enforce that $\mathcal{T}(\Psi)$ integrates to one for the term of interest in (18) and zero for the remaining terms. Following the SOLA approach, we define an objective function to be minimized, which comprises terms involved in the determination

of the estimate

$$\Theta = \oint_{S_C} [\mathcal{K}_C(\mathbf{r}_0|\mathbf{r}') - \mathcal{T}_C(\mathbf{r}_0|\mathbf{r}')]^2 \mathrm{d}S'_C + \oint_{S_C} [\mathcal{K}_{\dot{C}}(\mathbf{r}_0|\mathbf{r}') - \mathcal{T}_{\dot{C}}(\mathbf{r}_0|\mathbf{r}')]^2 \mathrm{d}S'_C + \oint_{S_M} [\mathcal{K}_M(\mathbf{r}_0|\mathbf{r}') - \mathcal{T}_M(\mathbf{r}_0|\mathbf{r}')]^2 \mathrm{d}S'_M + \lambda^2 \mathbf{q}^T \underline{\underline{\mathbf{E}}} \mathbf{q}, \tag{21}$$

where λ (units of $[\mathrm{nT}^{-1}]$) is a trade-off parameter and $\underline{\underline{\mathbf{E}}}$ is the data error covariance matrix that is necessary because the real geophysical problem involves noisy data. Which terms to include in the objective function depends on what we seek to estimate; for instance estimating the radial field over a time window short enough that field time-dependence can be ignored, means that the second term is not included. On the other hand estimation of the SV involves retaining the second term as well while setting the target kernels $\mathcal{T}_C$, $\mathcal{T}_M$ to zero. The diagonal elements of the data error covariance matrix are constructed from a combination of the QD latitude-dependent data error estimates, and Huber weights, w_n appropriate for a long-tailed error distribution (see Section 2)

$$\sigma^2_{w,n}(\theta_{QD}) = \frac{\sigma^2(\theta_{QD})}{w_n} \tag{22}$$

$$E_{ln} = \sigma^2_{w,n} e^{\frac{-\Delta t_{ln}}{\tau}}, \tag{23}$$

where the indices (l, $n = 1, ..., N$), $\Delta t_{ln} = t_l - t_n$ are data time differences and τ is the serial error correlation time set to 600 s based on the findings of Lowes and Olsen (2004). We note that the covariance matrix is symmetric (i.e. $E_{ln} = E_{nl}$) and positive definite. When deriving main field estimates using data taking along the satellite tracks at a sampling rate of 15 s, see Section 4.1, we multiply variances by a factor $\sin\theta$, where θ is geographic co-latitude, to account for there being more data close to the poles and in order to simulate an equal-area distribution (Olsen *et al.* 2014). For estimates of the SV, see Section 4.2, data are selected such that a good global coverage is obtained overthe chosen time window; in this case the differences in the data time are much longer than the correlation time and we are able to neglect the temporal correlation.

3.3 Numerical implementation

The minimization of the objective function (21) is performed by taking the derivative with respect to q_n,and requiring that $\partial\Theta/\partial q_n = 0$. Discretizing the integrals using a quadrature rule, the resulting set of equations subject to the constraint (17) may be written in the following form (Larsen & Hansen 1997)

$$\left[\underline{\underline{\mathbf{K}}}_C \underline{\underline{\mathbf{W}}} \underline{\underline{\mathbf{K}}}_C^T + \underline{\underline{\mathbf{K}}}_{\dot{C}} \underline{\underline{\mathbf{W}}} \underline{\underline{\mathbf{K}}}_{\dot{C}}^T + \underline{\underline{\mathbf{K}}}_M \underline{\underline{\mathbf{W}}} \underline{\underline{\mathbf{K}}}_M^T + \lambda^2 \underline{\underline{\mathbf{E}}}\right] \mathbf{q}(\mathbf{r}_0) = \underline{\underline{\mathbf{K}}}_C \underline{\underline{\mathbf{W}}} \mathbf{t}_C(\mathbf{r}_0) + \underline{\underline{\mathbf{K}}}_{\dot{C}} \underline{\underline{\mathbf{W}}} \mathbf{t}_{\dot{C}}(\mathbf{r}_0) + \underline{\underline{\mathbf{K}}}_M \underline{\underline{\mathbf{W}}} \mathbf{t}_M(\mathbf{r}_0) \tag{24}$$

$$\textit{subject to} \quad \left[\mathbf{e}_p^T \underline{\underline{\mathbf{W}}} \underline{\underline{\mathbf{K}}}_C^T + \mathbf{e}_p^T \underline{\underline{\mathbf{W}}} \underline{\underline{\mathbf{K}}}_{\dot{C}}^T + \mathbf{e}_p^T \underline{\underline{\mathbf{W}}} \underline{\underline{\mathbf{K}}}_M^T\right] \mathbf{q}(\mathbf{r}_0) = 1. \tag{25}$$

Here we define $\mathbf{K}$ matrices of size $N \times M$, where M is the size of the quadrature grid, such that

$$(\mathbf{K})_{np} = \left[G^*_{C,n}(\mathbf{r}_p), G^*_{\dot{C},n}(\mathbf{r}_p), G^*_{M,n}(\mathbf{r}_p)\right], \quad n = 1, ..., N \quad p = 1, ..., M \tag{26}$$

and $\mathbf{W}$ is a diagonal matrix of the integration points of size $M \times M$

$$(\mathbf{W})_{pp} = l_p, \quad p = 1, ..., M \tag{27}$$

and we have introduced the three vectors: $\mathbf{e}_p = (1, ..., 1)^T$, $\mathbf{t}(\mathbf{r}_0)$ having elements $(\mathbf{t}(\mathbf{r}_0))_p = \mathcal{T}(\mathbf{r}_0|\mathbf{r}_p)$ and $\mathbf{k}(\mathbf{r}_0)$ having elements $(\mathbf{k}(\mathbf{r}_0))_p = \mathcal{K}(\mathbf{r}_0|\mathbf{r}_p)$ for $p = 1, ..., M$. The discretized averaging kernel is calculated as $\mathbf{k}(\mathbf{r}_0) = \underline{\underline{\mathbf{K}}}^T \mathbf{q}(\mathbf{r}_0)$. The required angular integrations over the CMB and magnetosphere are performed numerically using Lebedev angular quadrature weights l_p on a grid $\mathbf{r}_p = (r_c, \theta_p, \phi_p)$ (Lebedev & Laikov 1999; Parrish 2010) that allow efficient calculation of integrals on a sphere

$$\int_S F(\mathbf{r}')\mathrm{d}S' \approx \sum_{p=1}^{M} l_p F(\mathbf{r}_p). \tag{28}$$

We found that using $M = 1730$ Lebedev points, corresponding to SH degree and order 71, were sufficient to perform the integrations to the required accuracy. We solve the normal equations for the coefficients, $\mathbf{q} = (q_1, ..., q_N)$, using a Lagrange multiplier ν as proposed by Pijpers & Thompson (1994)

$$\begin{pmatrix} \underline{\underline{\mathbf{K}}}_C \underline{\underline{\mathbf{W}}} \underline{\underline{\mathbf{K}}}_C^T + \underline{\underline{\mathbf{K}}}_{\dot{C}} \underline{\underline{\mathbf{W}}} \underline{\underline{\mathbf{K}}}_{\dot{C}}^T + \underline{\underline{\mathbf{K}}}_M \underline{\underline{\mathbf{W}}} \underline{\underline{\mathbf{K}}}_M^T + \lambda^2 \underline{\underline{\mathbf{E}}} & \underline{\underline{\mathbf{K}}}_C \underline{\underline{\mathbf{W}}} \mathbf{e}_p + \underline{\underline{\mathbf{K}}}_{\dot{C}} \underline{\underline{\mathbf{W}}} \mathbf{e}_p + \underline{\underline{\mathbf{K}}}_M \underline{\underline{\mathbf{W}}} \mathbf{e}_p \\ \mathbf{e}_p^T \underline{\underline{\mathbf{W}}} \underline{\underline{\mathbf{K}}}_C^T + \mathbf{e}_p^T \underline{\underline{\mathbf{W}}} \underline{\underline{\mathbf{K}}}_{\dot{C}}^T + \mathbf{e}_p^T \underline{\underline{\mathbf{W}}} \underline{\underline{\mathbf{K}}}_M^T & 0 \end{pmatrix} \begin{pmatrix} \mathbf{q}(\mathbf{r}_0) \\ \nu \end{pmatrix} =$$

$$\begin{pmatrix} \underline{\underline{\mathbf{K}}}_C \underline{\underline{\mathbf{W}}} \mathbf{t}_C(\mathbf{r}_0) + \underline{\underline{\mathbf{K}}}_{\dot{C}} \underline{\underline{\mathbf{W}}} \mathbf{t}_{\dot{C}}(\mathbf{r}_0) + \underline{\underline{\mathbf{K}}}_M \underline{\underline{\mathbf{W}}} \mathbf{t}_M(\mathbf{r}_0) \\ 1 \end{pmatrix}.$$

The first matrix term on the left-hand side is independent of estimate position $\mathbf{r}_0$. It therefore only needs to be computed once, significantly reducing the amount of computation required for producing a number of estimates at different locations. The linear system is solved for the vector containing $(q_1, ..., q_N, \nu)$, then the averages, the averaging kernels and the uncertainty estimates (variances) are computed. We note that alternative LSQR solution schemes could also be used to solve such systems (Larsen & Hansen 1997; Zaroli 2016). When estimating the radial MF at a given location, data from within a month is used, such that the term involving $\underline{\underline{\mathbf{K}}}_{\dot{C}}$ is neglected and the target kernel terms $\mathbf{t}_{\dot{C}}(\mathbf{r}_0)$, $\mathbf{t}_M(\mathbf{r}_0)$ are set to zero. When estimating the radial SV the target kernel terms $\mathbf{t}_C(\mathbf{r}_0)$, $\mathbf{t}_M(\mathbf{r}_0)$ are set to zero.

3.4 Appraisal of the constructed averages

A primary concern of the Backus–Gilbert method is the appraisal of solutions, that is to attain information regarding the resolvability offered by the magnetic field observations. A crucial insight is that the estimated average field is the only unique information offered by the data; that is, the estimated average along with the averaging kernel constitutes our knowledge of the field in the vicinity of the target location (Oldenburg 1984; Parker 1994). Appraisal typically consists of obtaining the averaging kernel, often described in terms of its width, together with the uncertainty of the average. Here, we define the kernel width to be the angular distance between points at which the averaging kernel reaches zero amplitude moving away from its maximum value (note that in contrast the original Backus–Gilbert method used the width as the full width at half maximum). We calculate the variance, $\widehat{\sigma}^2(\mathbf{r}_0, t_0)$, of the estimate of the radial field at location $(\mathbf{r}_0, t_0)$ propagated from the data error covariance matrix by

$$\widehat{\sigma}^2(\mathbf{r}_0, t_0) = \sum_{l,n}^{N} q_l E_{ln} q_n = \mathbf{q}^T \underline{\underline{E}} \mathbf{q}. \tag{29}$$

A family of solutions with different levels of trade-off between fitting the target function and obtaining an estimate with low variance is obtained; a small λ corresponds to fitting only the target function which decreases the width of the averaging kernel increasing the spatial resolution but at the expense of the statistical reliability (i.e. yielding a large variance and error magnification), while increasing λ broadens the averaging kernel lowering the spatial resolution, but produces a more reliable estimate (smaller variance). Note that contamination from averaging kernel side lobs and from leakage of co-estimated fields have not been included in the variance estimates described here.

4 RESULTS

Here we demonstrate our geomagnetic SOLA method in two applications: estimation of the radial component of the core field (Section 4.1) and estimation of the radial component of the secular variation (Section 4.2) at the CMB. Furthermore, we present computations of the change in the radial secular variation (i.e. the accumulated SA) from differences in SV estimates.

4.1 Application to the main field

We begin by illustrating the SOLA method by determining estimates of the radial core field at a sequence of target locations at the CMB using sums and differences of *Swarm* field measurements taken from March 2017 using data with a 15 sec sampling rate. Working with sums and differences of the vector field, the data vector is $\mathbf{d} = \{\Delta\mathbf{d}_r, \Sigma\mathbf{d}_r, \Delta\mathbf{d}_\theta, \Sigma\mathbf{d}_\theta, \Delta\mathbf{d}_\phi, \Sigma\mathbf{d}_\phi\}$. The data kernels are then constructed as

$$G^* = \left\{\Delta G_{C,r}, \Sigma G_{C,r}, \Delta G_{C,\theta}, \Sigma G_{C,\theta}, \Delta G_{C,\phi}, \Sigma G_{C,\phi}\right\},$$

where $\Delta G_{C,k} = [G_{C,k}(\mathbf{r}_1|\mathbf{r}') - G_{C,k}(\mathbf{r}_2|\mathbf{r}')]$ and $\Sigma G_{C,k} = [G_{C,k}(\mathbf{r}_1|\mathbf{r}') + G_{C,k}(\mathbf{r}_2|\mathbf{r}')]/2$ are data kernels for the differences and sums, respectively with $(k = r, \theta, \phi)$. Focusing solely on estimating the radial component of the core field and ignoring time-dependency, the second term is omitted from the objective function (21) and the constraint (18). Note that in this application, using magnetic data sampled every 15 sec, we have included an exponential serial data error covariance model and the equal area weighting factor as described in Section 3.2. In Fig. 3 we investigate the behaviour of the averaging kernel, $\mathcal{K}_C$, as a function of the target kernel width parameter κ and the trade-off parameter λ by considering a series of example averaging kernels at QD latitude 0° and longitude −168°. The plots provide the error estimate $\widehat{\sigma}$ for the field average and the kernel width in degrees. Increasing κ (i.e. going from left to right in the plot columns) causes the kernel to become narrower while increasing its amplitude and the variance. However, increasing κ induces more oscillations in the kernel structure around the target location. Increasing λ (i.e. going from top to bottom in the plot rows) decreases the kernel amplitude and increases its width, reducing the side lobe oscillations. In order to obtain a good resolution it is desirable to select a narrow, high amplitude, kernel, while at the same time trying to keep the side lobe oscillations to a minimum. The kernels are all well behaved showing only minor side lobes compared to the kernel amplitudes, hence we are motivated to push towards a high κ value. In general, we found that increasing the amount of data tends to decrease the width of the averaging kernel and lower the variance.

Next we consider how the SOLA method performs at four different QD latitudes: (0°, 35°, 70°, 85°). The reason for choosing these QD latitudes is to investigate the performance of the SOLA method in regions of external field disturbance with different amplitudes and different data coverage; in the Arctic region QD latitudes 70° and 85° are located approximately within and poleward of the auroral oval, respectively, while QD 35° represents mid-latitudes and QD 0° represents low-latitudes. The left-hand plot in Fig. 4 presents the local error

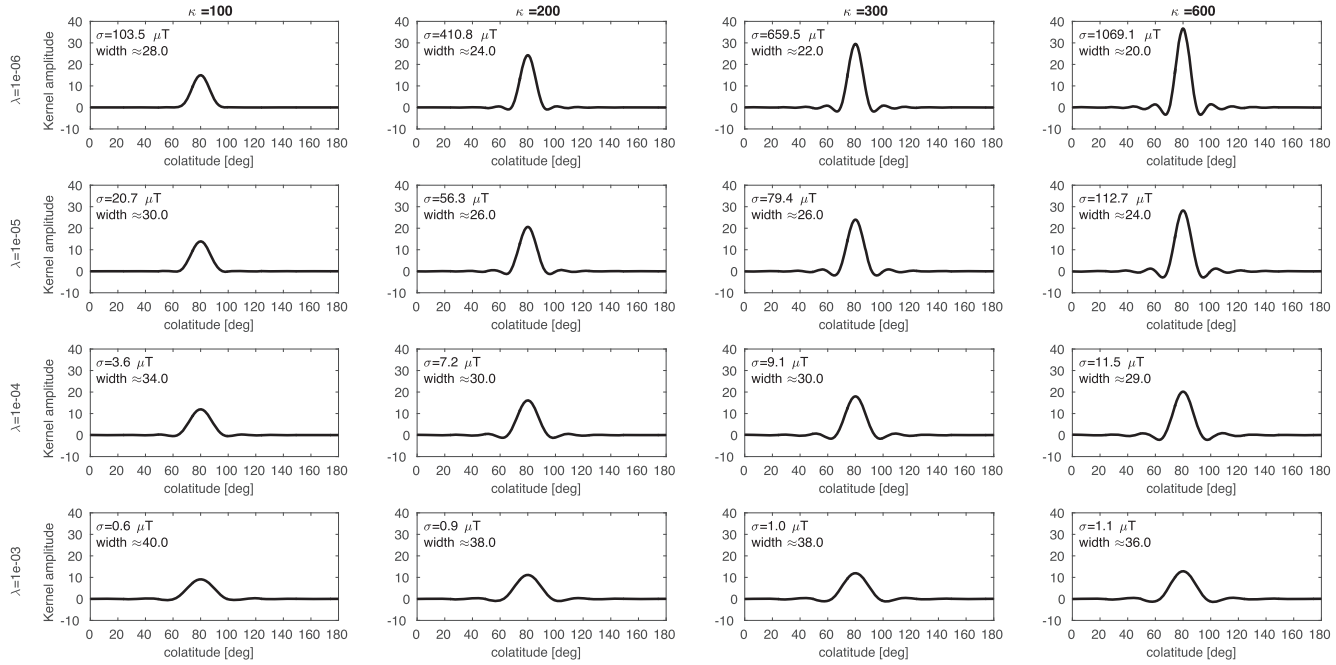

Figure 3. Main field application using data from March 2017 shown at target location with QD latitude 0°: behaviour of the averaging kernel as a function of Fisher function width κ and trade-off parameter λ. The value of κ increases from the left column having $\kappa = 100$ to the right column having $\kappa = 600$. The value of λ increases from the top row of $\lambda = 10^{-6}$ nT^{-1} to the bottom row having $\lambda = 10^{-3}$ nT^{-1}. In each plot the estimated uncertainty on the average, $\hat{\sigma}$,and kernel width in degrees are stated.

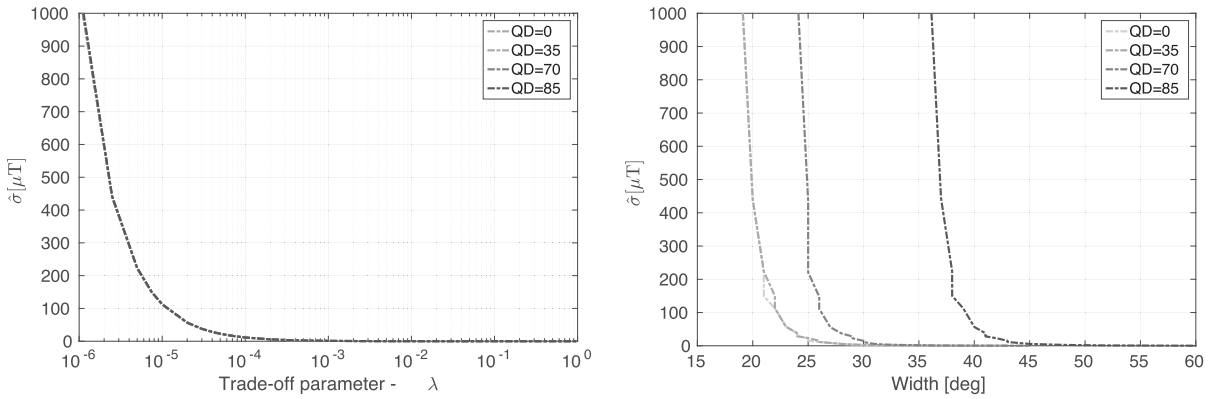

Figure 4. Main field application to the minimization problem eq. (21) using data from March 2017 for various target locations at QD latitudes 0°, 35°, 70° and 85°. Left-hand panel: local average error estimate $\hat{\sigma}(\mathbf{r}_0)$ versus trade-off parameter λ. Right-hand panel: local average error estimate $\hat{\sigma}(\mathbf{r}_0)$ versus main field averaging kernel width in degrees.

estimate versus the trade-off parameter λ.We find the size of the error estimates are of similar independent of the QD latitude for the various trade-off parameters. Hence, we may use the left-hand plot in Fig. 4 to pinpoint a suitable λ that yields more or less uniform error estimates for regional or global collections of point estimates. The right-hand plot in Fig. 4 presents the local error estimate versus the averaging kernel width in degrees, and shows a characteristic L-curve shape (the curves for latitudes 0° and 35° are coinciding). Here we note a right-shift of the L-curves as the QD latitude increases; for each curve the plot clearly illustrates how a low error estimate is associated with a large averaging kernel width and vice versa. The low and mid-latitude kernel widths are seen to be significantly smaller than in the auroral regions. This behaviour is expected since the data error estimates are larger in the auroral regions; hence to obtain the same variance the averaging kernel needs to become broader. Based on the information contained in Figs 3 and 4 we have chosen to use a Fisher's parameter $\kappa = 600$ and trade-off parameter $\lambda = 1 \times 10^{-4}$ nT^{-1} in the following calculations of the main field.

The top left plot in Fig. 5 presents a global collection of such radial field estimates at the CMB with a 1° spacing. Associated plots present the related error estimates (top right), the kernel widths (bottom left) and the data distribution under consideration (bottom right). We observe that the radial field patches and their amplitudes are very similar to those seen in the CHAOS-6-x7 field model predictions for SH degrees 1–13. Error estimates remain homogeneous as expected from Fig. 4. Kernel widths are seen to be more or less uniform at non-polar latitudes showing coherence with the data distribution, while distinct behaviour of the kernels is found in the polar regions; in particular, a striking region of increased kernel width coinciding with the auroral oval is observed as expected given the data error estimates shown in

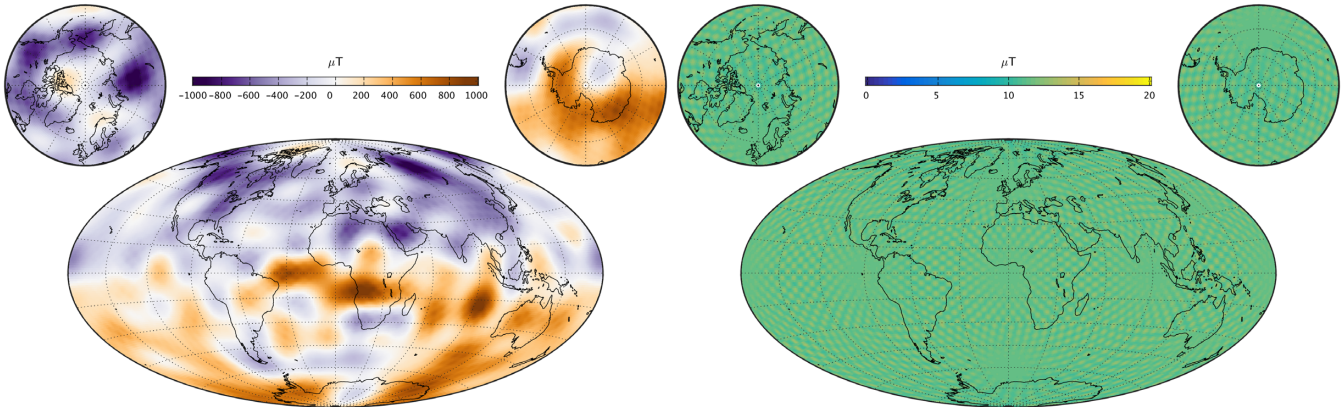

(a) Map collecting local estimates of CMB radial field $\widehat{B_r}(\mathbf{r}_0, t_0)$ in $[\mu\mathrm{T}]$.

(b) Map collecting local error estimates $\widehat{\sigma}(\mathbf{r}_0, t_0)$ in $[\mu\mathrm{T}]$.

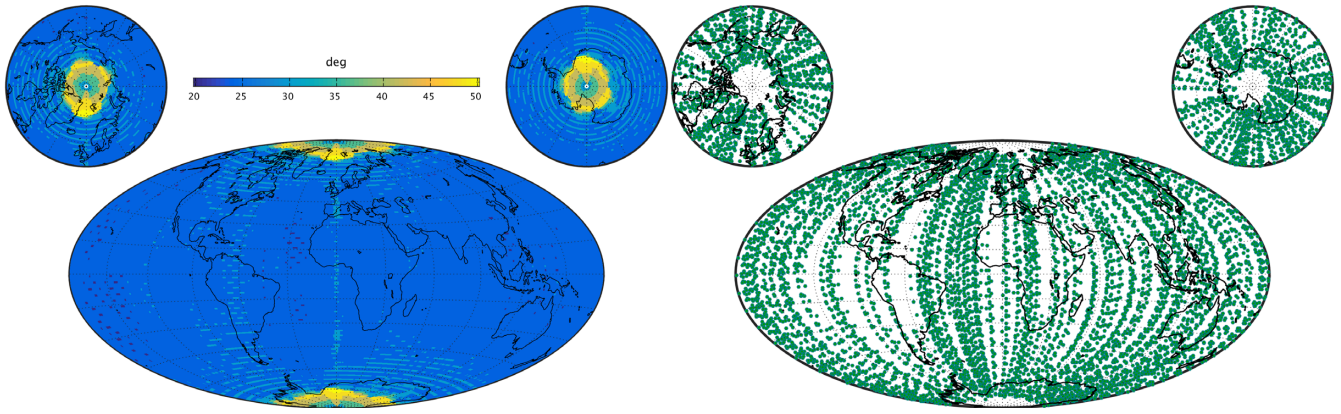

(c) Width of averaging kernel $\mathcal{K}_C(\mathbf{r}_0|\mathbf{r}')$ for local estimates in [deg].

(d) Location of observations used in March 2017 example.

Figure 5. Main field application using March 2017 *Swarm* data sums and differences using $\kappa = 600$ and $\lambda = 10^{-4}\ \mathrm{nT}^{-1}$ showing: (a) radial MF estimates at the CMB for a global 1° spaced collection of target locations, (b) uncertainty estimates for each target point, (c) averaging kernel widths for each target point and (d) *Swarm* data distribution.

Fig. 1. On the CMB, at radius r_c, the wavelength λ_n associated with a particular SH degree n is $\lambda_n = (2\pi r_c)/n$ ($1^\circ \approx 61$ km). Averaging kernels having widths of $\approx 30^\circ$ correspond approximately to SH degree 12. Hence, the resolution we obtain for the core field is comparable to that provided by conventional core field models, but note that each local estimate is the result of an individual inversion.

4.2 Application to the secular variation and accumulated secular acceleration

Next we illustrate an application of the SOLA method to the radial field secular variation at the CMB using a time window of 2 yr of *Swarm* vector field data from 2015.0 to 2017.0. Here we use only the radial field component of the satellite data in order to reduce external field contamination at high latitudes and in an effort to maximize the data coverage for a given number of data, such that the data vector is here $\mathbf{d} = \{\mathbf{d}_r\}$, and the data kernels are $G^* = \{G_{C,r}\}$. For 2 month time windows starting from 2015.0, we constructed a regularly spaced global distribution by randomly selecting data in time (within the 2 month window) on an equal area grid. A data set covering the period 2015.0 to 2017.0 was then generated by accumulating these 2 month data sets from the entire 2 yr, resulting in a total of 43 540 radial field data points. Here, serial error correlation in the data was not accounted for as data were selected randomly from within the 2 months. We start by considering the L-curve behaviour for the same QD positions investigated in the MF case. Fig. 6 presents the local error estimate versus the trade-off parameter λ (left-hand plot) and versus the averaging kernel width in degrees (right-hand plot). As in the MF case the error estimates are seen to be independent of location for a given λ value; for a given value of λ a corresponding $\widehat{\sigma}(\mathbf{r}_0)$ is fixed and we may read off the value of the kernel width at a given QD latitude. Furthermore, in both plots we mark blue, red and green dots for selected λ values studied in more detail in Figs 7 and 8. Here, we consider in detail three different λ values in order to investigate the resolvability of the SV with different choices of the average kernel. Fig. 7 shows examples of the averaging kernels obtained using $\lambda = 2.5 \times 10^{-4}\ \mathrm{nT}^{-1}$ (the blue dot in Fig. 6) top left-hand plot, $\lambda = 5 \times 10^{-4}\ \mathrm{nT}^{-1}$ (the red dot in Fig. 6) top right-hand plot and $\lambda = 5 \times 10^{-3}\ \mathrm{nT}^{-1}$ (the green dot in Fig. 6) bottom plot, having widths of $\approx 30^\circ$, 33° and 42°; comparing the three kernels it is clear that using $\lambda = 2.5 \times 10^{-4}\ \mathrm{nT}^{-1}$ results in higher amplitudes and a narrower averaging kernel. Fig. 8 presents a global collection of radial field SV estimates at the CMB having a 1° spacing on the left and associated kernel widths on the right, here shown for $\lambda = 2.5 \times 10^{-4}\ \mathrm{nT}^{-1}$ in the top plots, $\lambda = 5 \times 10^{-4}\ \mathrm{nT}^{-1}$ in the centre plots and $\lambda = 5$

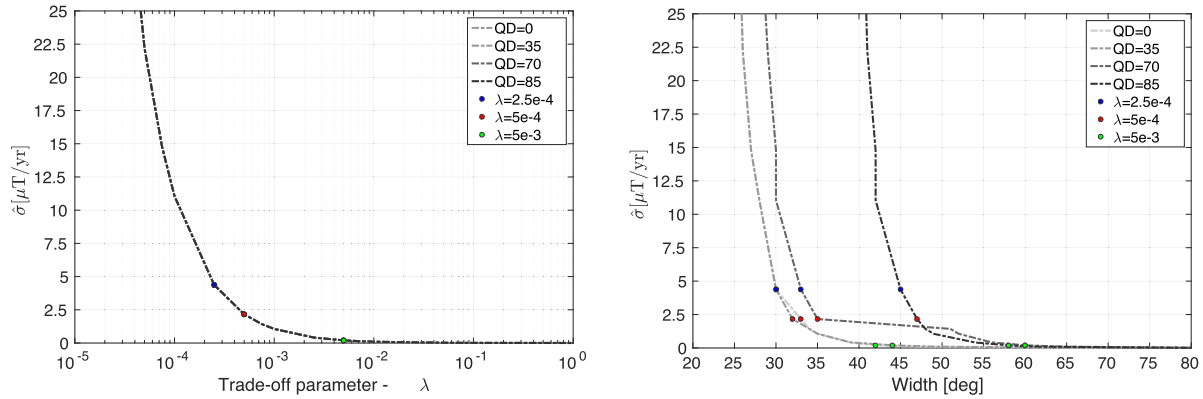

Figure 6. SV radial field application to the minimization problem eq. (21) using 2 yr of *Swarm* data between 2015.0 and 2017.0 having $\kappa = 600$. Plots showing $\widehat{\sigma}(\mathbf{r}_0)$ trade-off curves at various target locations for QD latitudes 0°, 35°, 70° and 85° as a function of λ (left-hand panel) and kernel width (right-hand panel).

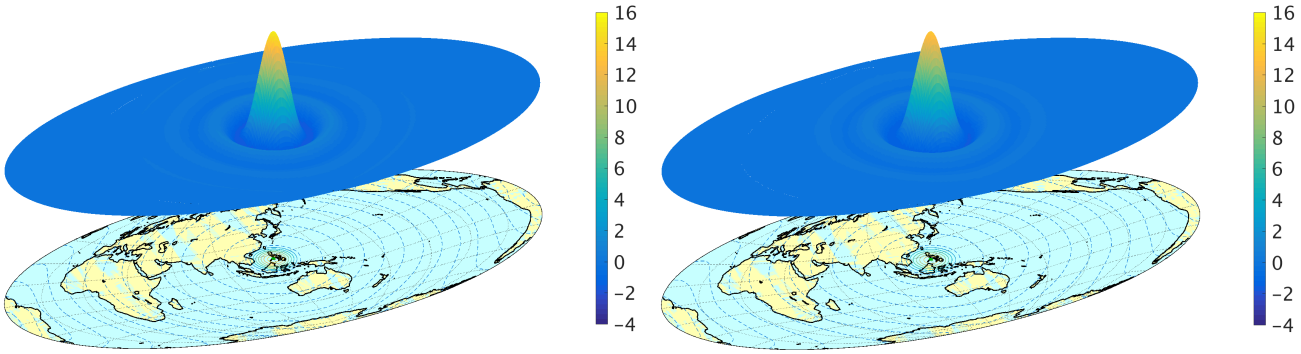

(a) SV averaging kernel for $\lambda = 2.5 \times 10^{-4}\mathrm{nT}^{-1}$. Kernel width ≈ 30°.

(b) SV averaging kernel using $\lambda = 5 \times 10^{-4}\mathrm{nT}^{-1}$. Kernel width ≈ 33°.

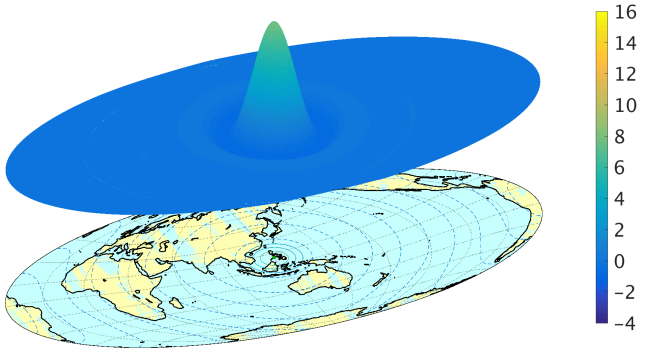

(c) SV averaging kernel using $\lambda = 5 \times 10^{-3}\mathrm{nT}^{-1}$. Kernel width ≈ 42°.

Figure 7. SV radial field application using 2 yr of *Swarm* data between 2015.0 and 2017.0 having $\kappa = 600$. Plots show example kernels at target location QD latitude 0° for : (a) $\lambda = 2.5 \times 10^{-4}$ nT^{-1}, (b) $\lambda = 5 \times 10^{-4}$ nT^{-1} and (c) $\lambda = 5 \times 10^{-3}$ nT^{-1} marked with blue, green and red dots in Fig. 6, respectively. The green dot in the map locates the kernel centre. Contour interval is 2.0. Negative contours are dashed.

$\times 10^{-4}$ nT^{-1} in the bottom plots. The effect of changing λ, and thus the averaging kernel, is clearly seen in the these plots: the field structures become smeared out as the kernel width is increased (i.e. going from top plots to bottom plots), decreasing the amplitude while a decrease in the associated error estimates is also observed. The kernel width increases towards the polar regions resembling the results in the MF case study, peaking at areas matching those of the auroral oval.

Remembering that our method involves no explicit spectral regularization of higher spatial frequencies of the signal, it is interesting to compare our global SV estimates to SV field predictions of the CHAOS-6-x7 model. Though the method, as well as the data and the data selection criteria, are not the same in the two approaches, similar SV structures can clearly be identified; in particular high amplitude features appearing at low latitudes stretching over a longitudinal band of ±90°, lower activity in the pacific region (at least for the broader averaging kernels) and a sequence of high latitude patches encircling the north pole. Though decreasing kernel width may cause noise to become more influential in the average estimate, in particular at mid-latitudes and polar regions, a clear change in the eastern pacific region is evident for λ

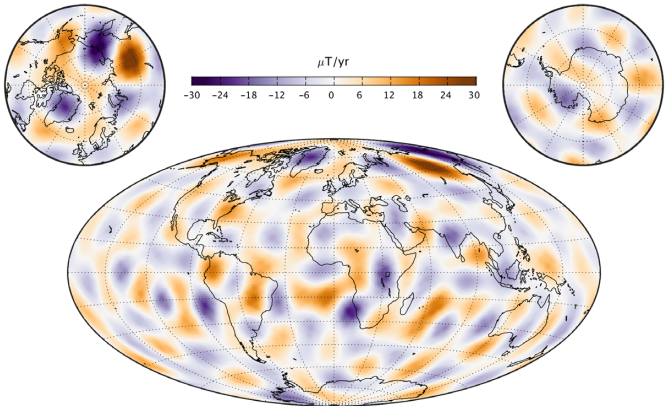

(a) Local estimates of CMB radial SV for $\lambda = 2.5 \times 10^{-4}$. $\widehat{\sigma} \approx 5\mu T/yr$.

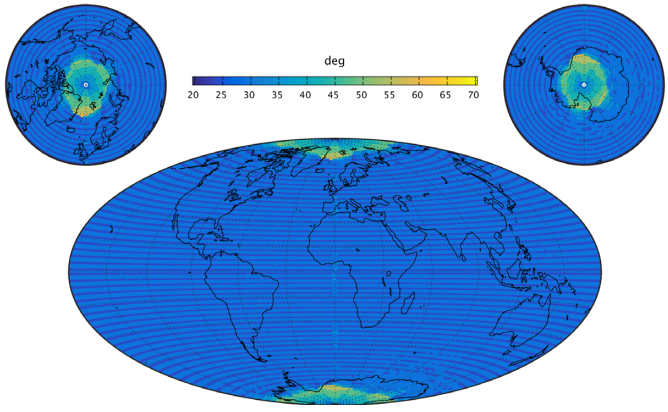

(b) Width of averaging kernel using $\lambda = 2.5 \times 10^{-4}\mathrm{nT}^{-1}$.

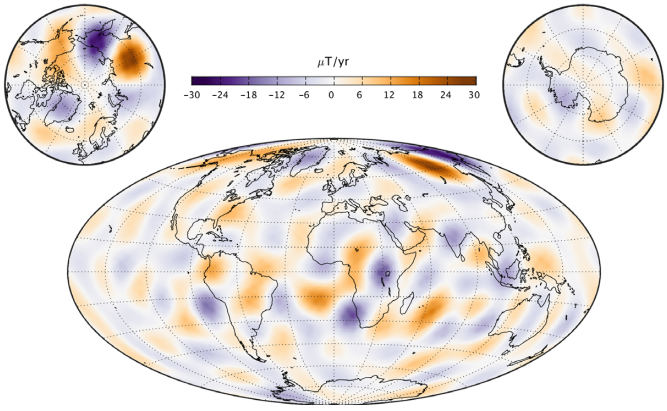

(c) Local estimates of CMB radial SV for $\lambda = 5 \times 10^{-4}\mathrm{nT}^{-1}$. $\widehat{\sigma} \approx 2.5\mu T/yr$.

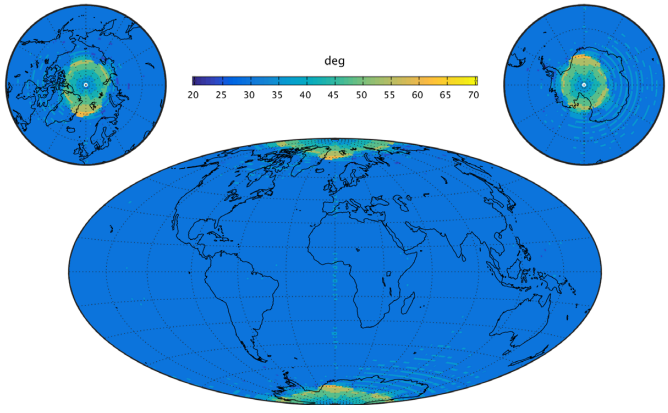

(d) Width of averaging kernel using $\lambda = 5 \times 10^{-4}\mathrm{nT}^{-1}$.

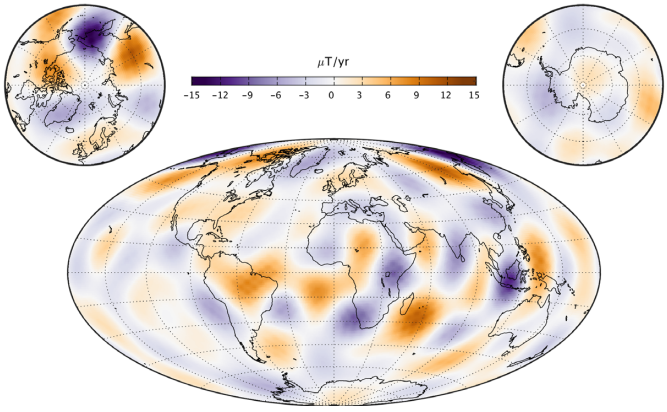

(e) Local estimates of CMB radial SV for $\lambda = 5 \times 10^{-3}$. $\widehat{\sigma} \approx 0.25\mu T/yr$.

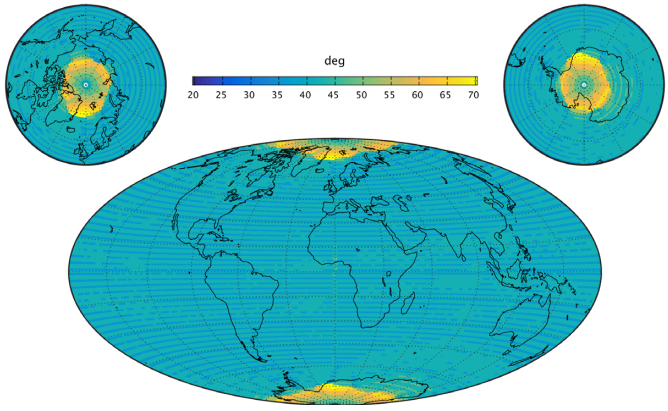

(f) Width of averaging kernel using $\lambda = 5 \times 10^{-3}$.

Figure 8. SV radial field application using 2 yr of *Swarm* data between 2015.0 and 2017.0 showing a global collection of target points (1° spacing) having $\kappa = 600$. Results shown are: (a and b) using $\lambda = 2.5 \times 10^{-4}$ nT^{-1}, (c and d) using $\lambda = 5 \times 10^{-4}$ nT^{-1} and (e and f) using $\lambda = 5 \times 10^{-3}$ nT^{-1}.

$= 2.5 \times 10^{-4}$ nT^{-1}, which is interesting as recent SH based field models find distinct SA features in this region (Chulliat *et al.* 2015; Finlay *et al.* 2016).

Fig. 9 reports the radial SA computed as the accumulated change in the radial SV between years 2015 to 2017, 2007 to 2009 and 2005 to 2007. To determine this, the SV in 2017.0 was computed from 2 yr of data (as above) using $\lambda = 5 \times 10^{-3}$ nT^{-1}; that is, seeking SV maps having detail levels as given in Fig. 8(e). In a second step, the averaging kernels determined using this value of λ, were used as the target kernels for the SV in 2005, 2007 and 2015.0 in order to ensure the quantities to be differenced have been averaged in the same fashion. Finally the accumulated SA was computed as the difference in SV between 2005 and 2007, respectively 2015 and 2017. Comparing such maps of the accumlated SA with the SA predictions of the CHAOS-6-x7 model up to SH degree 10, the SOLA maps agree well with the CHAOS-6 model predictions. Even small scale field features can be found in both models, though the high latitude SA signal is perhaps not as prominent in the SOLA maps. Thus the SA predictions of regularized SH based models up to SH degree 10 are essentially reproduced by our approach.

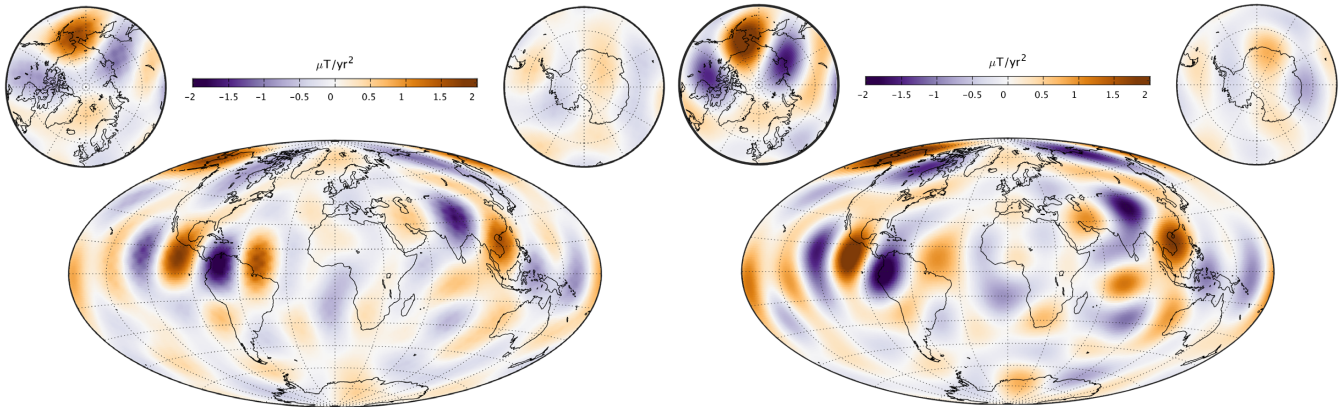

(a) Radial SA in 2016.0 based on $\lambda = 5 \times 10^{-3}\mathrm{nT}^{-1}$. $\widehat{\sigma} \approx 0.16\mu\mathrm{T/yr}^2$.

(b) Radial SA from CHAOS-6-x7 in 2016.0 based on SH degrees 1-10.

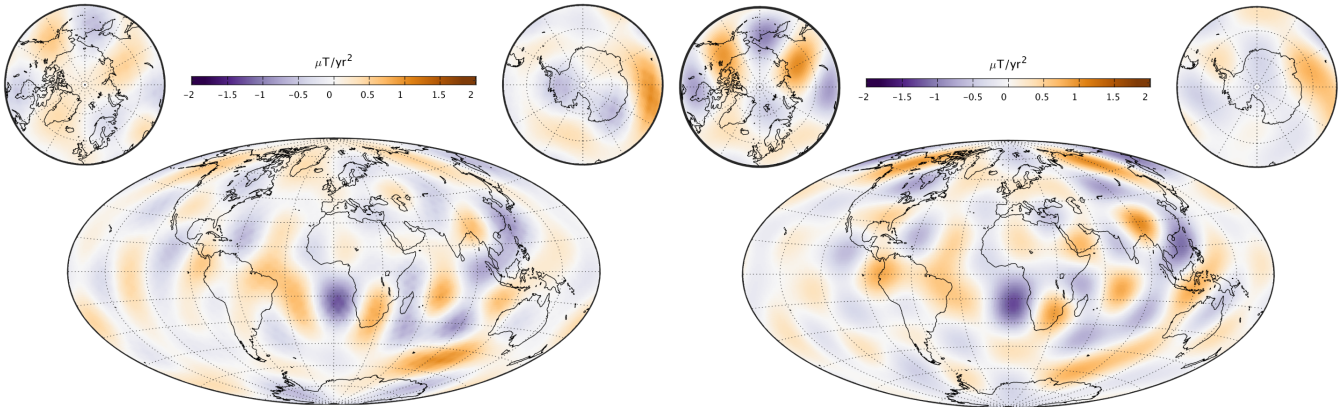

(c) Radial SA in 2008.0 based on $\lambda = 5 \times 10^{-3}\mathrm{nT}^{-1}$. $\widehat{\sigma} \approx 0.18\mu\mathrm{T/yr}^2$.

(d) Radial SA from CHAOS-6-x7 in 2008.0 based on SH degrees 1-10.

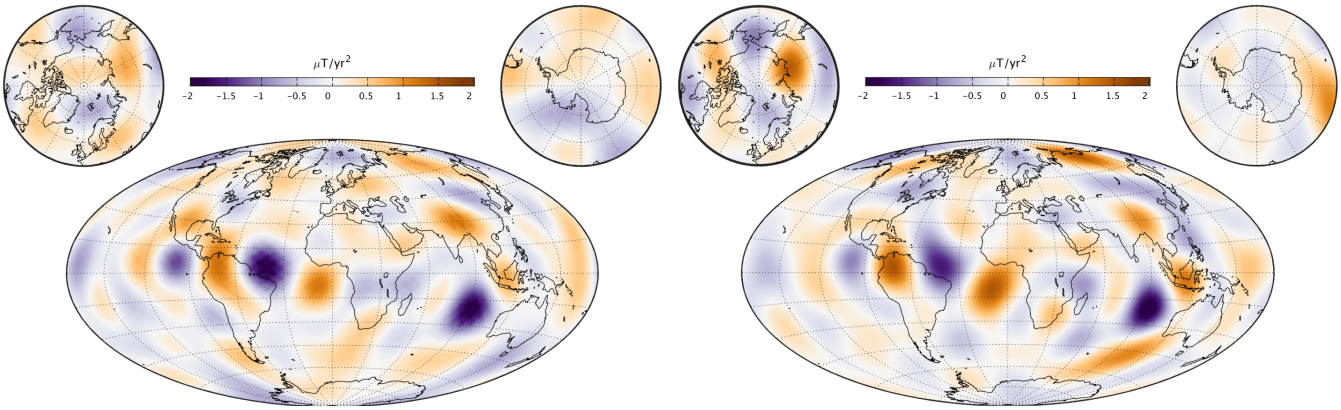

(e) Radial SA in 2006.0 based on $\lambda = 5 \times 10^{-3}\mathrm{nT}^{-1}$. $\widehat{\sigma} \approx 0.25\mu\mathrm{T/yr}^2$.

(f) Radial SA from CHAOS-6-x7 in 2006.0 based on SH degrees 1-10.

Figure 9. SA computed as accumulated change in radial SV at the CMB from: (a) years 2015−2017, (c) years 2007–2009 and years 2005–2007 using $\lambda = 5 \times 10^{-3}\,\mathrm{nT}^{-1}$. Plots (b), (d) and (f) show the CHAOS-6-x7 model SA predictions truncated at SH degree 10 for years 2016, 2008 and 2006 at the CMB, respectively.

The evolution of the radial SA at the CMB is shown in Fig. 10, presenting time-longitude plots along the geographic equator as determined using our approach. Here we have experimented by looking at 1 and 2 yr SV differences derived from data windows sliding in steps of 1 and 2 month s, respectively. The reason for not showing results prior to 2004 in plots (c) and (d) is that using a 1 month sliding time window causes a severe lack of data during this time with our data selection criteria. The left-hand plots show the SA evolution at the equator while the right-hand plots show corresponding error estimates. From plots (a) and (c) coherent evolving structures are observed. This is important as it illustrates the ability of our method to track temporal changes. As can be seen, much higher temporal resolution is gained in (c) using 1 yr SV differences. Associated uncertainty estimates show an increase in amplitude between 2004 and 2005, which is likely related to there being less data at this time. Striped looking patterns in the error estimates can be seen, which are probably related to the regular spatial grid of the selected data . This behaviour may be reduced by seeking a different data grid setup. The SA patterns observed in

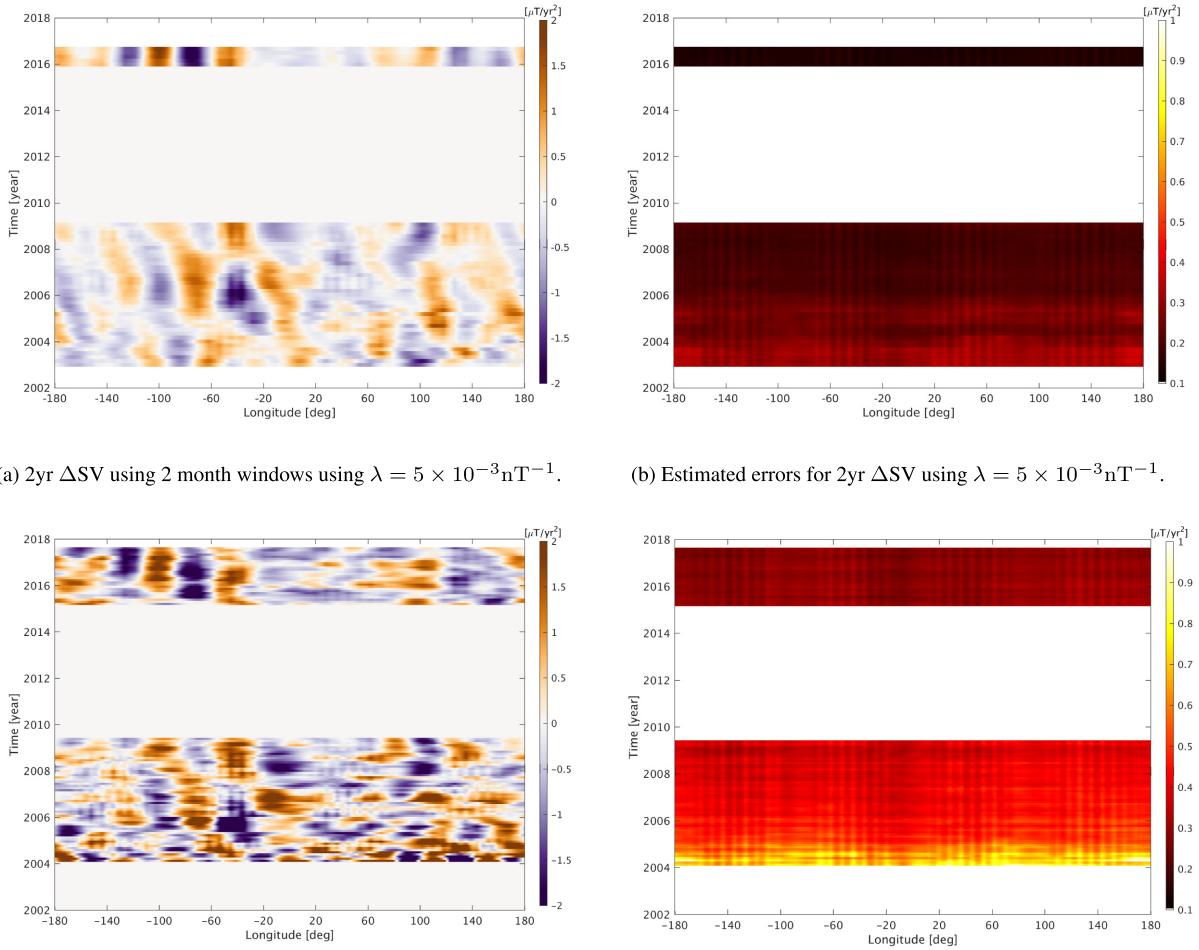

(a) 2yr ΔSV using 2 month windows using $\lambda = 5 \times 10^{-3}\mathrm{nT}^{-1}$.

(b) Estimated errors for 2yr ΔSV using $\lambda = 5 \times 10^{-3}\mathrm{nT}^{-1}$.

(c) 1yr ΔSV using 1 month windows using $\lambda = 5 \times 10^{-3}\mathrm{nT}^{-1}$.

(d) Estimated errors for 1yr ΔSV using $\lambda = 5 \times 10^{-3}\mathrm{nT}^{-1}$.

Figure 10. Time-longitude plot of the accumulated SA along the geographical equator at the CMB. Showing (a) Difference of SV estimates 2 yr apart, each derived over a 2 yr window, windows moving in 2 month steps, and derived using $\lambda = 5 \times 10^{-3}$ nT^{-1}, (b) uncertainty estimates for plot (a), (c) Difference of SV estimates 1 yr apart, each derived over a 1 yr window, windows moving in 1 month steps, again using $\lambda = 5 \times 10^{-3}$ nT^{-1}, (d) uncertainty estimates for plot (c).

plots (a) and (c), correspond qualitatively to those found in the CHAOS-6 model and in previous studies (Chulliat *et al.* 2015); in particular the prominent features appearing between 2005 and 2009 in the longitude band from -100° to 20°.

5 DISCUSSION AND CONCLUSION

We have presented an application of the modified Backus-Gilbert formalism called SOLA, originally developed in helioseismology, to determine local average estimates of the core-generated magnetic field and its time derivatives. These estimates are in good agreement with maps of the CMB radial MF, SV and SA derived using conventional spherical harmonic modelling techniques.

The Backus–Gilbert formalism offers a useful alternative approach to retrieving information on the geomagnetic field in comparison to conventional field modelling; instead of relying on a truncated and regularized spherical harmonic representation being downward continued to the CMB, we average over the field directly at the CMB and thus obtain unbiased estimates. An important advantage of our method is that it automatically provides the spatial averaging kernels and variances associated with the estimates thus allowing for a detailed appraisal of the field averages; a range of well-characterized solutions can be realized by varying the target kernel width via the trade-off parameter λ; it is desirable to have a low target width while at the same time having a sufficiently low uncertainty estimate for the field averages. In contrast it is not straight-forward to provide variances for point estimates at the CMB field derived from truncated and regularized SH models, and workers rarely compute the associated spatial averaging kernels. An advantage of SOLA compared to regularized least-squares inversion is that the variance estimates are not artificially suppressed. The Backus–Gilbert estimate can in some circumstances be closer to the true value than the least-squares solution, provided the quantity being estimated (in our case the radial field at the CMB, $B_r(\mathbf{r}', t)$) is sufficiently smooth (Parker 1977; Pujol 2013). Although the Backus–Gilbert approach was not originally intended for global model construction, the union of a

collection of point estimates has been considered by some authors to constitute a sensible approach (e.g. Parker 1994; Nolet 2008). In principle a trade-off curve could be calculated for each location under consideration. We have instead selected one value for the trade-off parameter for all locations, so the variances of the estimates and the kernel widths can vary with position reflecting for example uneven data distribution or enhanced data errors in regions such as the auroral zone. Although the kernel width provides only a very crude summary of the actual averaging scale (Parker 1994), for the satellite data considered here with their good global coverage, it is found to be a useful diagnostic. Our averaging kernels are generally well behaved when using the same trade-off parameter for all locations, having averaging kernels without significant side lobes (amplitudes are less than 10 per cent of the kernel peak amplitude). The possibility also exists of pre-specifying other target kernels in order to estimate a particular form of spatial average; here we have chosen for simplicity to focus on a Fisher distribution but other possibilities including for example a disc boxcar averaging function are possible depending on the desired application.

We obtained stable and spatially coherent local estimates of both the MF and SV at the CMB. Using 2 yr of data it is possible to make stable SV maps at the CMB with averaging widths as small as 30°, a wavelength similar to a SH representation up to degree 12. The SV is thus known at this wavelength without regularization. Motivated by this we went a step further and determined the accumulated SA between two epochs by differencing the SV estimates for the epochs. The resulting maps of radial SA at the CMB were found to be in good agreement with the CHAOS-6-x7 field model truncated at degree 10. By varying the width of the spatial averaging kernel, and observing the change in the resulting maps and their variance estimates, we can directly appraise how well the accumulated SA is known, something that has up to now been difficult to assess in regularized field models. We carry out our SA estimates locally, so we are able to find the optimal spatial averaging width for a specific location and time window of interest, without worrying that the inversion might be unstable due to high amplitude noise in some other region. This enables us to study in detail rapid field changes in particular locations. Looking at time-longitude plots of the accumulated SA at the equator, we have explored the coherence of the accumulated SA as the width of the averaging kernel is decreased, and the time window is shortened. We find encouraging coherence at the equator down to an averaging width of 30°, and for accumulated SA within 1 yr based on 1 yr time windows for the SV. This may be a sign that we are unveiling a coherent underlying signal, albeit one that has more power on shorter wavelengths (see also Holme *et al.* 2011; Aubert 2018). Note that since no spectral truncation is carried out, higher spatial frequencies in our estimates may have a different appearance than that found in SH based models such as CHAOS-6 where temporal regularization is known to heavily influence the SA above SH degree 9so the SA is often analysed by truncating or filtering above this degree (e.g. Chulliat *et al.* 2015; Finlay *et al.* 2016). As an example, considering the accumulated SA at the equator derived from 1 yr differences in the SV estimates, we find a distinctive 'cross-over' feature in mid 2007 at 25° West. This involves two adjacent and oppositely directed radial SA features that change sign within a year. Estimates of the accumulated SV made using longer time windows show a more gradual evolution, and perhaps westward motions, as a result of smearing between patches on either side of the cross over. The SA cross-over is more clearly seen for shorter time windows, confirming hints at its presence in models such as CHAOS-6 (Chulliat *et al.* 2015). The origin of such features, that may involve a rapid change in sign of the azimuthal core flow acceleration (Gillet *et al.* 2015) may reveal new aspects of core dynamics, so it is important that their characteristics are robustly determined. The method presented here is well suited to such investigations.

One shortcoming of the SOLA method at present is that it requires the solution of a linear system of size (number of data x number of data). For large numbers of data locations, as are available from satellite missions, this can becomes prohibitive, especially if one wishes to consider single satellite and inter-satellite sums and differences for each vector field component at each location. As the results presented here show, the problem is not insurmountable, particularly if one is only interested in field estimates within a short time window, or is willing to perform data decimation in order to obtain a data set with good spatial and temporal coverage. If we wish to push towards higher local resolution in space and time, it is clear that using data sets that are as large as possible can be an advantage. Despite this, the major source of error in the present determination of the core field is probably the incomplete separation of crustal and ionospheric signals. Since our method is based on a potential field formulation, it is unable to perform such a separation with data from satellite altitude alone; bias from incompletely separated non-core field sources cannot be excluded in the maps we have presented and is difficult to quantify. Including data from several altitudes will help, as will experiments carried out for different external field selection criteria.

Having established here the utility of the SOLA approach in geomagnetism, there are now a number of interesting possibilities for future applications. First, as the time-series collected by the *Swarm* mission lengthens, there will be more and more rapid field evolution events that can be studied in detail. The ability to appraise inferred core field features will be especially important as we seek to study the temporal evolution of small scale SA signals on shorter and shorter timescales, in an effort to understand the underlying geophysical processes. Moving further back in time, the method could be applied to data from other satellite missions such as DMSP (Alken *et al.* 2014) or Cryosat to try to fill the gap between the CHAMP and *Swarm* era. The method could be also be applied to ground observatory magnetic data; this would be of particular interest in regions such as Europe, North America and Australia where there is excellent coverage with ground-based observatories. This would provide an opportunity to study the local field evolution at high resolution and provide an important means of validating results obtained with satellite data. The method could also be applied to produce local estimates at locations other than the CMB, for example on a grid at mean satellite altitudes, as an alternative method of producing so-called virtual observatories (Mandea & Olsen 2006). Field estimates on regular grids with suitable averaging and variance information would certainly be well suited for data assimilation applications. Looking further afield, it may also be possible to apply the method in archeomagnetism and palaeomagnetism where the data coverage is even more sparse, and appraisal information would again be valuable. As an example, perhaps the SOLA method could be used to study what is happening at the CMB during archeomagnetic intensity spike events (Ben-Yosef *et al.* 2009; Shaar *et al.* 2016; Korte & Constable 2018), although this would require linearization approaches in order to deal with non-linear intensity and directional data (e.g. Snieder 1991). The

ability to study core field features directly from observations, independent of regularized spherical harmonic field models or other *a priori* constraints, seems to be attractive for a broad range of applications.

ACKNOWLEDGEMENTS

The authors would like to thank Nils Olsen for providing various Matlab tools including those to determine the CM4 ionospheric model predictions and the internal/external CHAOS-6-x7 model predictions. We wish to thank Kathy Whaler for helpful discussions on the Backus–Gilbert method. We would also like to thank Aslak Stubsgaard for helpful discussions regarding computational considerations. We thank the GFZ German Research Centre for Geoscience for providing access to the CHAMP MAG-L3 data and ESA for providing access to the *Swarm* L1b MAG-L data. High resolution 1-min OMNI data was provided by the Space Physics Data Facility (SPDF), NASA Goddard Space Flight Centre. The Lebedev integration was performed using a Matlab function by Parrish (2010). The exponential correlation model was build using the Matlab tool Synthetic_Variogram by T. Mejer-Hansen. This project was supported by the The Danish Council for Independent Research, Natural Sciences (grant DFF 4002-00366). The financial support is gratefully acknowledged.

REFERENCES

Alken, P., Maus, S., Lühr, H., Redmon, R., Rich, F., Bowman, B. & O'Malley, S., 2014. Geomagnetic main field modeling with DMSP, *J. geophys. Res.: Space Phys.,* **119**(5), 4010–4025.

Aubert, J., 2018. Geomagnetic acceleration and rapid hydromagnetic wave dynamics in advanced numerical simulations of the geodynamo, *Geophys. J. Int.,* **214**(1), 531–547.

Backus, G. & Gilbert, F., 1968. The resolving power of gross Earth data, *Geophys. J. Int.,* **16**(2), 169–205.

Backus, G. & Gilbert, F., 1970. Uniqueness in the inversion of inaccurate gross Earth data, *Phil. Trans. R. Soc. Lond., A: Math. Phys. Eng. Sci.,* **266**(1173), 123–192.

Backus, G., Parker, R. & Constable, C., 1996. *Foundations of Geomagnetism,* Cambridge Univ. Press.

Barton, G., 1989. *Elements of Green's Functions and Propagation: Potentials, Diffusion, and Waves,* Oxford Univ. Press.

Ben-Yosef, E., Tauxe, L., Levy, T.E., Shaar, R., Ron, H. & Najjar, M., 2009. Geomagnetic intensity spike recorded in high resolution slag deposit in Southern Jordan, *Earth planet. Sci. Lett.,* **287**(3), 529–539.

Bloxham, J., Gubbins, D. & Jackson, A., 1989. Geomagnetic secular variation, *Phil. Trans. R. Soc. Lond., A,* **329**(1606), 415–502.

Bouligand, C., Gillet, N., Jault, D., Schaeffer, N., Fournier, A. & Aubert, J., 2016. Frequency spectrum of the geomagnetic field harmonic coefficients from dynamo simulations, *Geophys. Suppl. Mon. Not. R. Astron. Soc.,* **207**(2), 1142–1157.

Chulliat, A. & Maus, S., 2014. Geomagnetic secular acceleration, jerks, and a localized standing wave at the core surface from 2000 to 2010, *J. geophys. Res.: Solid Earth,* **119**(3), 1531–1543.

Chulliat, A., Alken, P. & Maus, S., 2015. Fast equatorial waves propagating at the top of the Earth's core, *Geophys. Res. Lett.,* **42**(9), 3321–3329.

Constable, C. & Parker, R., 1988. Smoothing, splines and smoothing splines; their application in geomagnetism, *J. Comput. Phys.,* **78**(2), 493–508.

Constable, C.G., Parker, R.L. & Stark, P.B., 1993. Geomagnetic field models incorporating frozen-flux constraints, *Geophys. J. Int.,* **113**(2), 419–433.

Constable, C., 1988. Parameter estimation in non-Gaussian noise, *Geophys. J. Int.,* **94**(1), 131–142.

Finlay, C.C., Olsen, N., Kotsiaros, S., Gillet, N. & Tøffner-Clausen, L., 2016. Recent geomagnetic secular variation from Swarm and ground observatories as estimated in the CHAOS-6 geomagnetic field model, *Earth, Planets Space,* **68**(1), 1–18.

Fisher, R., 1953. Dispersion on a sphere, *Proc. R. Soc. Lond., A: Math., Phys. Eng. Sci.,* in , Vol. **217,** pp. 295–305, .

Gillet, N., Jault, D., Finlay, C. & Olsen, N., 2013. Stochastic modeling of the Earth's magnetic field: inversion for covariances over the observatory era, *Geochem., Geophys., Geosyst.,* **14**(4), 766–786.

Gillet, N., Jault, D. & Finlay, C., 2015. Planetary gyre, time-dependent eddies, torsional waves, and equatorial jets at the Earth's core surface, *J. geophysi. Res.: Solid Earth,* **120**(6), 3991–4013.

Gubbins, D. & Roberts, N., 1983. Use of the frozen flux approximation in the interpretation of archaeomagnetic and palaeomagnetic data, *Geophys. J. Int.,* **73**(3), 675–687.

Holme, R., Olsen, N. & Bairstow, F., 2011. Mapping geomagnetic secular variation at the core–mantle boundary, *Geophys. J. Int.,* **186**(2), 521–528.

Holschneider, M., Chambodut, A. & Mandea, M., 2003. From global to regional analysis of the magnetic field on the sphere using wavelet frames, *Phys. Earth planet. Inter.,* **135**(2-3), 107–124.

Holschneider, M., Lesur, V., Mauerberger, S. & Baerenzung, J., 2016. Correlation-based modeling and separation of geomagnetic field components, *J. geophys. Res.: Solid Earth,* **121**(5), 3142–3160.

Jackson, A., Constable, C., Walker, M. & Parker, R., 2007. Models of Earth's main magnetic field incorporating flux and radial vorticity constraints, *Geophys. J. Int.,* **171**(1), 133–144.

Korte, M. & Constable, C.G., 2018. Archeomagnetic intensity spikes: global or regional geomagnetic field features? *Front. Earth Sci.,* **6,** 17.

Kotsiaros, S., Finlay, C. & Olsen, N., 2015. Use of along-track magnetic field differences in lithospheric field modelling, *Geophys. J. Int.,* **200**(2), 878–887.

Langel, R.A., 1987. The main field, in *Geomagnetism,* Vol. **1,** pp. 249–512, ed. Jacobs, J.A., Academic Press.

Larsen, R.M. & Hansen, P.C., 1997. Efficient implementations of the SOLA mollifier method, *Astron. Astrophys. Suppl. Ser.,* **121**(3), 587–598.

Lebedev, V.I. & Laikov, D., 1999. A quadrature formula for the sphere of the 131st algebraic order of accuracy, in *Doklady. Mathematics,* Vol. **59,** pp. 477–481, MAIK Nauka/Interperiodica.

Lesur, V., Wardinski, I., Rother, M. & Mandea, M., 2008. Grimm: the GFZ Reference Internal Magnetic Model based on vector satellite and observatory data, *Geophys. J. Int.,* **173**(2), 382–394.

Lesur, V., Wardinski, I., Baerenzung, J. & Holschneider, M., 2017. On the frequency spectra of the core magnetic field Gauss coefficients, *Phys. Earth planet. Inter.*

Louis, A.K. & Maass, P., 1990. A mollifier method for linear operator equations of the first kind, *Inverse Problems,* **6**(3), 427.

Lowes, F. & Olsen, N., 2004. A more realistic estimate of the variances and systematic errors in spherical harmonic geomagnetic field models, *Geophys. J. Int.,* **157**(3), 1027–1044.

Mandea, M. & Olsen, N., 2006. A new approach to directly determine the secular variation from magnetic satellite observations, *Geophys. Res. Lett.,* **33**(15) .

Masters, G. & Gubbins, D., 2003. On the resolution of density within the Earth, *Phys. Earth planet. Inter.,* **140**(1), 159–167.

Nolet, G., 2008. *A Breviary of Seismic Tomography: Imaging the Interior of the Earth and Sun,* Cambridge Univ. Press.

Oldenburg, D.W., 1984. An introduction to linear inverse theory, *IEEE Trans. Geosci. Rem. Sens.,* **GE-22**(6), 665–674.

Olsen, N. *et al.*, 2015. The Swarm initial field model for the 2014 geomagnetic field, *Geophys. Res. Lett.,* **42**(4), 1092–1098.

Olsen, N. & Mandea, M., 2008. Rapidly changing flows in the Earth's core, *Nat. Geosci.,* **1**(6), 390.

Olsen, N., Mandea, M., Sabaka, T.J. & Tøffner-Clausen, L., 2009. CHAOS-2—a geomagnetic field model derived from one decade of continuous satellite data, *Geophys. J. Int.*

Olsen, N., Lühr, H., Finlay, C.C., Sabaka, T.J., Michaelis, I., Rauberg, J. & Tøffner-Clausen, L., 2014. The CHAOS-4 geomagnetic field model, *Geophys. J. Int.,* **197**(2), 815–827.

Olsen, N., Finlay, C.C., Kotsiaros, S. & Tøffner-Clausen, L., 2016. A model of Earth's magnetic field derived from 2 years of Swarm satellite constellation data, *Earth, Planets Space,* **68**(1), 124.

Parker, R.L. & Shure, L., 1982. Efficient modelling of the Earth's magnetic field with harmonic splines, *Geophys. Res. Lett.,* **9,** 812–815.

Parker, R.L., 1977. Understanding inverse theory, *Ann. Rev. Earth planet. Sci.,* **5**(1), 35–64.

Parker, R.L., 1994. *Geophysical Inverse Theory,* Princeton Univ. Press.

Parrish, R., 2010. Matlab code: getlebedevsphere.

Pijpers, F. & Thompson, M., 1992. Faster formulations of the optimally localized averages method for helioseismic inversions, *Astron. Astrophys.,* **262,** L33–L36.

Pijpers, F. & Thompson, M., 1994. The SOLA method for helioseismic inversion, *Astron. Astrophys.,* **281,** 231–240.

Plattner, A. & Simons, F.J., 2017. Internal and external potential-field estimation from regional vector data at varying satellite altitude, *Geophys. J. Int.,* **211**(1), 207–238.

Pujol, J.M., 2013. The Backus-Gilbert method and their minimum-norm solution, *Geophysics,* **78**(3), W9–W30.

Richmond, A., 1995. Ionospheric electrodynamics using magnetic apex coordinates., *J. Geomagnet. Geoelectr.,* **47**(2), 191–212.

Ritter, P., Lühr, H., Maus, S. & Viljanen, A., 2004. High-latitude ionospheric currents during very quiet times: their characteristics and predictability, *Ann. Geophys.*, **22,** 2001–2014.

Sabaka, T.J., Olsen, N. & Purucker, M.E., 2004. Extending comprehensive models of the Earth's magnetic field with Ørsted and CHAMP data, *Geophys. J. Int.,* **159**(2), 521–547.

Shaar, R., Tauxe, L., Ron, H., Ebert, Y., Zuckerman, S., Finkelstein, I. & Agnon, A., 2016. Large geomagnetic field anomalies revealed in Bronze to Iron Age archeomagnetic data from Tel Megiddo and Tel Hazor, Israel, *Earth planet. Sci. Lett.,* **442,** 173–185.

Shure, L., Parker, R.L. & Backus, G.E., 1982. Harmonic splines for geomagnetic modelling, *Phys. Earth planet. Inter.,* **28,** 215–229.

Snieder, R., 1991. An extension of Backus-Gilbert theory to nonlinear inverse problems, *Inverse Problems,* **7**(3), 409.

Tanimoto, T., 1985. The Backus-Gilbert approach to the three-dimensional structure in the upper mantle-I. Lateral variation of surface wave phase velocity with its error and resolution, *Geophys. J. Int.,* **82**(1), 105–123.

Whaler, K. & Gubbins, D., 1981. Spherical harmonic analysis of the geomagnetic field: an example of a linear inverse problem, *Geophys. J. Int.,* **65**(3), 645–693.

Whaler, K.A., 1984. Fluid upwelling at the core-mantle boundary—resolvability from surface geomagnetic data, *Geophys. J. Int.,* **78**(2), 453–473.

Zaroli, C., 2016. Global seismic tomography using Backus–Gilbert inversion, *Geophys. Suppl. Mon. Not. R. Astron. Soc.,* **207**(2), 876–888.